Auckland Volcanic Field Seismicity

Meegan Soulsby

2023

ENVPHYS 780A/B
Word count: 11485

A thesis submitted to The University of Auckland in partial fulfilment of the requirements for the degree of Bachelor of Science (Honours) in Environmental Physics

Abstract

Auckland/Tāmaki Makaurau is New Zealand's most populated city; however, alongside its >1.6 million occupants, it hosts 53 late Quaternary volcanic edifices dating between $\sim$ 193 ka and $\sim$ 500 cal. yrs. BP which form the Auckland Volcanic Field (AVF). Despite being the focus of numerous studies, several questions remain regarding the formation of this intraplate volcanic field, including the lithospheric structure. Recent tomography studies have made significant progress in developing a 3D model of the lithospheric structure, revealing a NNW-SSE split in crustal velocity. However, seismic events in the Auckland region are yet to be located using such a model, emphasising how interpretations of their locations and, in turn, the crustal fault network, are likely severely limited. Consequently, GeoNet's catalogue of documented events surrounding the AVF are utilised in this study. In reviewing this catalogue, several events were either reclassified or rejected entirely. In addition, all events required adjustment and supplementation of P- and S-wave arrival picks for stations within the Auckland Volcanic Seismic Network (AVSN). Using these updated arrivals in NonLinLoc, a non-linear, probabilistic earthquake location algorithm, the most representative 1D homogeneous model was found (V_p = 5.94 km/s and V_s = 3.39 km/s). Relative to locations produced by GeoNet, those presented here are considerably more accurate, reflected in the average RMS reducing from 0.403 $\pm$ 0.3 s to 0.118 $\pm$ 0.06 s. Using this updated catalogue in the homogeneous model also unveiled spatiotemporal seismicity patterns related to known faults and a cluster of 19 events proximal to Rangitoto, which nucleated between 2012 and 2016. The residuals of individual stations also portray the same crustal velocity dichotomy as previous work. Future development of a 3D crustal model for the AVF seismicity catalogue is likely to migrate these events nearer toward known faults such as the Whangaparoa Passage, Islington Bay, and Te Puru faults.

Acknowledgements

Contents

List of Tables

List of Figures

1 Introduction

The Auckland Volcanic Field (AVF) is an intraplate volcanic field, manifesting itself in the distinctive topography of New Zealand's Auckland/Tāmaki Makaurau (Figure 1) (Hopkins et al., 2021). Although the exact number of volcanic centres within this monogenetic field has been debated, the current consensus is 53, with activity initiating ~193 ka with the formation of Lake Pupuke, to the most recent eruption of Rangitoto ~500 cal. yrs. BP (Hopkins et al., 2021; Leonard et al., 2017; Needham et al., 2011).

In terms of the number of centres, the AVF is considered one of the smallest global volcanic fields; however, regardless, it has been the focus of numerous studies (Hopkins et al., 2021). The decision to invest in constraining volcanism in the AVF is illuminated by Tāmaki Makaurau being the most populated city in New Zealand, hosting >1.6 million individuals (Statistics New Zealand, 2018). However, Hopkins et al. (2021) emphasise that gaps persist in our understanding of crucial factors such as mantle melting, ascent rates, the lithospheric structure, and controls on eruptive volumes and periods of inactivity. From a hazard and risk management perspective, these gaps accentuate the necessity for continued investigations, especially given the high population of potentially vulnerable people.

In this investigation, the emphasis is placed on refining our understanding of the lithospheric structure, expanding on the findings of previous research (e.g., Ashenden et al., 2011; Ensing, 2020; Ensing et al., 2022; Ganefianto, 2018; Horspool et al., 2006; Kenny et al., 2012). To achieve this, the study presented focuses on building upon our knowledge of seismicity in Auckland, given the potential to delineate crustal faults and contribute to subsurface imaging.

As such, a methodical, multi-step process is introduced, beginning with the initial step in the earthquake locating process: revising GeoNet's catalogue of documented events. This refinement involves improving and supplementing the P- and S-wave seismic phase arrival picks for stations within the Auckland Volcanic Seismic Network (AVSN) for each event in the catalogue (Figure 1). This is fundamental for the inversion process of earthquake locating, leading to optimising for the most representative crustal velocity model using the non-linear algorithm of NonLinLoc (Lomax et al., 2000).
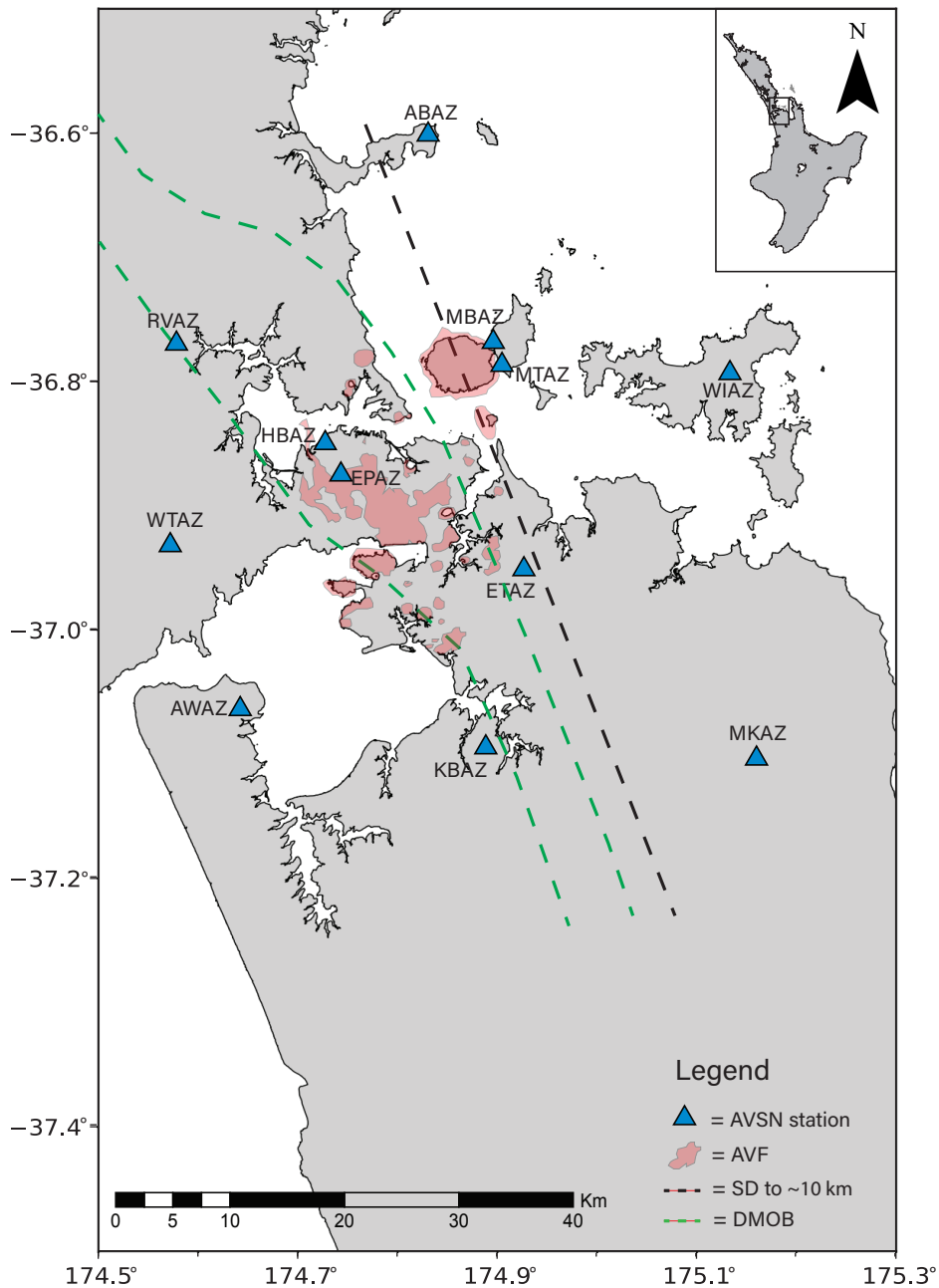
Figure 1: Map showing the extent of this study on the Auckland Volcanic Field (AVF) seismicity. The locations of the Auckland Volcanic Seismic Network (AVSN) of Table 1 are labelled, as well as the extent of the AVF deposits as indicated in Hopkins et al. (2021). The black dashed line is the shear wave velocity discontinuity (SD) to ∼ 10 km depth from Ensing (2020) and Ensing et al. (2022). Within the green dashed lines is the approximate position of the Dun Mountain Ophiolite Belt (DMOB) as estimated from Eccles et al. (2005).

The aim of obtaining the "best" velocity model is defined in this study by four key criteria. Firstly, it should locate earthquakes and quarry blasts near known faults and quarries. In addition, it should correlate with the known geological setting and minimise location quality metrics, including the weighted root-mean-square (RMS) misfit and the arrival residuals of individual stations.

2 Background

2.1 Geological and tectonic setting

New Zealand is renowned for its dynamic tectonic setting, located at the intersection of the Australian and Pacific Plates. Over geologic time, the relative plate motions producing the current configuration of this boundary and the arrangement of the countries' basement terranes have been equally as dynamic (e.g., Bradshaw, 1989; Sutherland, 1999). However, regarding the AVF, only the recent tectonic and geological settings are discussed here, given that volcanism is confined to the Quaternary (see Hopkins et al., 2021 for a review of preferred ages).

Offshore of the North Islands' eastern coastline, the boundary between these two tectonic plates is one of convergence, with the southwards transition of the Tonga-Kermadec Trench into the Hikurangi Margin characterised by subduction of the Pacific Plate beneath the overriding Australian Plate. Such subduction zones are well acquainted with the formation of volcanic arcs, generally aligned parallel to the plate boundary azimuth (e.g., Stern, 2002). Considering only the surface morphology of the AVF, there is, therefore, an evident detachment from association with arc-type magmatism. Instead, the Taupo Volcanic Zone (TVZ) embodies the on-land expression of New Zealand's currently active volcanic arc (e.g., Cole, 1990; Seebeck et al., 2013). Relative to the AVF, regions like the TVZ, which are closer to this subduction interface, have a better handle on the sources of volcanism, seismicity, and the crustal structure. Several datasets reflect this, such as the GNS Science active fault map, which highlights just five faults active since 25 ka in the AVF, compared to the hundreds of active tectonic surfaces in the thrust, dextral, and normal fault belts aligned westward of the Hikurangi Subduction Zone (GNS Science, 2023). Although the volume of active faults and the seismic moments that they are capable of nucleating will always be greater proximal to this major plate boundary, the 363 events occurring between 1992 and 2022, which

3

GeoNet has located in the surrounding Auckland area, highlights a severe lack of understanding of the fault network underlying this city. With eruption locations favouring pre-existing faults, this illuminates the importance of resolving the AVF's crustal structure through seismic studies like that presented here (e.g., Eccles et al., 2005; Kenny et al., 2012; Luthfian et al., 2023; Spörli et al., 2015).

Earthquake locating and interpretation of Auckland's fault network fundamentally relies on creating a velocity model that correlates with the known geological setting. As such, the three main basement terranes underlying the AVF are pivotal. The first of these is the Dun Mountain Ophiolite Belt, a NNW-SSE striking assemblage that truncates the Murihiku and Waipapa Terranes to the west and east, respectively (see Fig. 7. in Eccles et al., 2005).

2.2   Previous Research

Preceding studies on the AVF have primarily been carried out under the collaborative research programme DEtermining VOlcanic Risk in Auckland (DEVORA) (e.g., Deligne et al., 2019; Ensing et al., 2022; Gasston et al., 2021; Hopkins et al., 2021; Needham et al., 2011). Such multidisciplinary research integrates perspectives from geochemistry, geology, geophysics, and geoengineering, among other appropriate fields.

Regarding seismic studies, the intraplate setting of the AVF and the resultant low level of seismicity has influenced the use of methods like ambient noise tomography or teleseismic events to constrain the crustal structure (e.g., Ensing et al., 2022; Horspool et al., 2006). Horspool et al. (2006) identified a low shear wave velocity zone, which they attributed to partial melt residing at 70 - 90 km depth. Although geochemical analysis by McGee et al. (2013) supports this depth estimate as a magmatic source, it is crucial to note that this low-velocity zone finding has low resolution, based on data from just one seismic station, MKAZ. More recently, Ensing (2020) and Ensing et al. (2022) have used ambient noise tomography to construct a 3D shear wave speed model for the AVF, producing a much higher resolution crustal image than the model of Horspool et al. (2006). However, unlike the work of Horspool et al. (2006), this 3D model only reaches a depth of 25 km, although it has been instrumental in revealing the severe heterogeneity of Auckland's subsurface, once again delineating the central Dun Mountain Ophiolite Belt (Figure 1).

As shown in Deligne et al. (2019), earthquakes within the AVF generally nucleate within the uppermost 15 km of the crust, coinciding with the first four horizontal slices of Ensing (2020) and Ensing et al. (2022). To $\sim$ 10 km depth, an abrupt vertical discontinuity in shear wave speed has been identified (see Fig. 6 in Ensing et al., 2022). The NNW-SSE strike of this lineament correlates with that of the Dun Mountain Ophiolite Belt; however, it instead resides on the eastern margin of the AVF, underlying Rangitoto Volcano (Figure 1). A former primary wave travel-time tomography study also revealed a similar crustal dichotomy (Ganefianto, 2018). Such research accentuates how a custom, 3D velocity model for the AVF may be required to get the most accurate microseismic event locations, justifying or advancing fault maps like that of Kenny et al. (2012). Consequently, as mentioned, this investigation revises GeoNet's AVF seismicity catalogue, from which the "best" homogeneous model for earthquake relocation was optimised. Utilising location quality metrics produced by this simplest-case crustal model, the proposed velocity discontinuity has now been assessed outside of tomography.

2.3 Theoretical background

2.3.1 Wave propagation in an elastic medium

The wave equation is a second-order partial differential equation and arguably one of physics' most fundamental and universal mathematical statements. Although this relationship comes in various forms due to its utility across numerous specialisations such as optics, fluid mechanics, and electromagnetism, the seismological wave equation describes wave propagation in an elastic, isotropic medium and is an essential principle regarding earthquake locating (e.g., Stein and Wysession, 2013). Such a medium is defined by its material properties being directionally uniform and capable of returning to its original state once a wave-induced disturbance has passed – a simplification for the Earth's seismogenic zone that builds upon the 1D wave equation for a string (e.g., Stein and Wysession, 2013).

Considering only wave propagation, rather than accounting for the generating source, Newton's Second Law of Motion, $\mathbf{F} = m\mathbf{a}$, can be transformed into the equation of motion for an elastic solid (e.g., Stein and Wysession, 2013). In addition to this equation, reflecting on both dilatation

and the stress and strain of an isotropic solid permits the derivation of the elastic wave equation in a 3D, isotropic medium (Equation 1).

$$\rho\frac{\partial^2 \mathbf{u}(\mathbf{x},t)}{\partial t^2} = (\lambda + \mu)\nabla(\nabla \cdot \mathbf{u}(\mathbf{x},t)) + \mu\nabla^2\mathbf{u}(\mathbf{x},t) \tag{1}$$

Equation 1 is written in terms of displacement, $\mathbf{u}$, showing a clear dependence on both space ($\mathbf{x}$) and time (t). Additionally, two elastic constants are required, with this form written for the Lamé constant and shear modulus.

Instead of directly solving Equation 1, $\mathbf{u}$ can be written with reference to potentials. Equation 2 portrays this through the dependence of displacement on the scalar and vector potentials, $\phi(\mathbf{x},t)$ and $\boldsymbol{\gamma}(\mathbf{x},t)$, respectively (e.g., Stein and Wysession, 2013).

$$\mathbf{u}(\mathbf{x},t) = \nabla\phi(\mathbf{x},t) + \nabla \times \boldsymbol{\gamma}(\mathbf{x},t) \tag{2}$$

Within Equation 2, $\phi(\mathbf{x},t)$ and $\boldsymbol{\gamma}(\mathbf{x},t)$ satisfy the scalar and vector wave equations, Equations 3 and 4 respectively. As alluded to in Equation 2, $\phi(\mathbf{x},t)$ experiences dilatation or convergence, while $\boldsymbol{\gamma}(\mathbf{x},t)$ is instead connected with rotation by association of the curl (e.g., Stein and Wysession, 2013). With $\alpha = V_p$, and $\beta = V_s$, these results yield equations describing the velocities of compressional waves (V_p), and transverse waves (V_s) (Equations 5 and 6).

$$\nabla^2\phi(\mathbf{x},t) = \frac{1}{\alpha^2}\frac{\partial^2\phi(\mathbf{x},t)}{\partial t^2}, \text{where } \alpha = V_p \tag{3}$$

$$\nabla^2\boldsymbol{\gamma}(\mathbf{x},t) = \frac{1}{\beta^2}\frac{\partial^2\boldsymbol{\gamma}(\mathbf{x},t)}{\partial t^2}, \text{where } \beta = V_s \tag{4}$$

$$V_p = \sqrt{\frac{\lambda + 2\mu}{\rho}} \tag{5}$$

$$V_s = \sqrt{\frac{\mu}{\rho}} \tag{6}$$

Compressional and transverse waves are respectively known as primary waves (P-waves) and

shear waves (S-waves), arguably the two most commonly referred to seismic phases. With P-waves being purely longitudinal, disturbances within the elastic medium induce particle vibrations in the direction of wave propagation, resulting in a lack of polarization. Contrastingly, as announced, S-wave motions are not described by the same dilatational mechanisms but rather by particle motions perpendicular to the direction of wave propagation. Consequently, S-waves are characterised by two orthogonal polarizations.

As Equations 5 and 6 highlight, under any given scenario of elastic constants, V_p will always be greater than V_s, hence the "primary" annotation. This attribute manifests throughout this study, with P-wave arrivals always picked as the first disturbance from an ambient background noise level on a given seismograph.

3 Methods

3.1 Package installation

Prior to the undertaking of methods used to achieve this investigation aim, primary packages Miniconda and NonLinLoc were installed (Anaconda Software Distribution, 2022; Lomax et al., 2000).

3.2 Station inventory

Miniconda's accession allowed Python's seismic processing and analysing tool ObsPy to be installed, enabling access to The International Federation of Digital Seismograph Network (FDSN) (Beyreuther et al., 2010). In a jupyter notebook, the FDSN provides GeoNet, the New Zealand-wide seismometer network managed by GNS Science, to be used as a client, facilitating the acquisition of seismic station and earthquake data.

To access this information, specific spatial and temporal criteria must be predefined. This study specified the time frame from the beginning of 2012 to the present. This starting year was chosen given its simultaneity with GeoNet's implementation of SeisComP3, whereby both NonLinLoc and LOCSAT have been utilised, alongside the nz3drx and iasp91 velocity models, for earthquake locating (GeoNet, 2022). Given that this study compares GeoNet event locations with those re-

produced, this subsurface model consistency that a start date of 2012 provides supports the most meaningful correlations to be made.

The spatial extents were defined as those of the AVF, with latitudes and longitudes between -37.5°to -36.5°and 174.5°to 175.3°, respectively (Figure 1). This search placed twelve seismic stations within GeoNet's Auckland Volcanic Seismic Network (AVSN) in the station inventory, defined as those from ABAZ to WTAZ in Table 1. However, as evident in Table 1, additional broadband seismometers GRZ, KUZ, and TOZ were manually added following a "Sensor Map Search" in GeoNet's website, given their potential to reduce the model null space in future work. This procedure granted information, including depth, elevation, and location coordinates of the fifteen stations in and around the AVF, to be saved in a .txt file for use in NonLinLoc (Table 1). Furthermore, it initiated the process of building the catalogue of earthquakes used in this study.

Table 1: Seismic stations within the AVSN, as input into NonLinLoc. Positive depth values are down in the z-direction, while positive elevation values are up along this axis. GRZ, KUZ, and TOZ within the NZ Seismograph Network are also included, given that P- and S-wave picks have also been made on their waveforms. Picks made on these further afield stations are not utilised in this study but are likely to be in future work.

Station ID	Latitude (°)	Longitude (°)	Depth (km)	Elevation (km)
		AVSN		
ABAZ	-36.6	174.832	0	0.074
AWAZ	-37.064	174.643	0.371	0.103
EPAZ	-36.875	174.744	0.383	0.04
ETAZ	-36.953	174.928	0.347	0.195
HBAZ	-36.85	174.73	0.38	0.02
KBAZ	-36.095	174.889	0.16	0.012
MBAZ	-36.769	174.898	0.93	0.06
MKAZ*	-36.104	175.161	0	0.14
MTAZ	-36.786	174.906	0	0.065
RVAZ	-36.77	174.579	0.25	0.059
WIAZ	-36.793	175.134	0	0.255
WTAZ	-36.932	174.573	0	0.34
		NZ Seismograph Network		
GRZ*	36.250	175.458	0	0.146
KUZ*	-37.064	174.643	0	0.076
TOZ*	-36.875	174.744	0	0.085
Broadband seismometer				

3.3 Event catalogue

To build a catalogue of seismic events, the same spatiotemporal scales previously defined were searched within the GeoNet client; however, further criteria were also required.

With seismometers in the AVSN generally being 3-component, recording subsurface motions along three mutually perpendicular axes, stations listed in Table 1 tend to have three channels upon which waveform data is plotted; one in the vertical, or z-direction, and two in the two orthogonal horizontal azimuths. Thus, one of these criteria was to constrain the instrument type, sampling rate, and bandwidth. The search, therefore, was restricted to either high broadband or extremely short-period sensors measuring weak motions (e.g., velocity) at frequencies at or above 80 Hz. These sensor types were specified as "HH*" or "EH*." The "*" delineates that all orientations were searched given that equipment can be easily rotated, moving the z-axis away from being perpendicular to the Earth's surface as a result; a commonality in boreholes in which stations in Table 1 with depths greater than 0 km are placed.

Furthermore, the catalogue was defined to be ordered by descending magnitude, enabling events of the largest seismic moment, and thus those with the greatest potential for having both P -and S-wave picks on the maximum number of stations, to be made first to get a better-trained eye for this art. Section 3.4 describes this process of seismic phase arrival picking; however, a minimum magnitude of 1 was decided as the lower end-member to maximise the number of accurate picks for use in NonLinLoc for probabilistic event locating.

From this search criteria, 91 events were found within GeoNet's catalogue, in the defined spatiotemporal extent of the study.

3.4 Arrival picking

Of foundational to locating these 91 events within GeoNet's database was first to observe their respective waveform data across all stations and justify whether they are, in fact, seismic events with clear seismic phase arrivals or if, instead, they are to be rejected from the catalogue.

9

3.4.1 STA/LTA

Misinterpreted "events" are possible to arise where SeisComP3's automated picking method, short-term/long-term average (STA/LTA) performed through the 'scautopick' command, has occurred with a lack of manual review (Helmholtz-Centre Potsdam - GFZ German Research Centre for Geosciences and gempa GmbH, 2008).

In regions such as the AVF where local seismicity is low magnitude and anthropogenic noise is high, STA/LTA for seismic phase arrival picking is common practice given that it searches for places in each station stream where the signal-to-noise ratio (SNR) exceeds a certain threshold. This automatic method enhances the monitoring and locating of large data sets but requires the user to pre-define four key variables: the STA, LTA, and trigger and detrigger thresholds.

The STA represents the "instantaneous" seismic signal, which requires the established time window to be short enough to maximise the triggering of lower-frequency local events, but long enough to still be sensitive to the shortest events likely in the location of interest. Contrastingly, the LTA encapsulates the average amplitude of background noise before the arrival of seismic phases. In the case of the AVF, the longer the LTA window, the greater the likelihood of discriminating local events above the triggering threshold, which determines those recorded in GeoNet's initial catalogue for manual review vs. those not. The triggering threshold is an upper limit on the STA/LTA ratio, determining when a pick will be made. The detrigger threshold, therefore, delineates a lower STA/LTA ratio at which triggering is activated again, resetting the system to search for further waveform anomalies. In the AVF, the triggering threshold set by GeoNet must be small enough to pick up lower amplitude events but not too large, as false "events" that, in reality, represent background noise could be triggered. Comparatively, the detriggering threshold must be set low enough to prevent the triggering routine from re-establishing multiple times throughout an event but high enough to prevent the trigger from being active longer than the event lasts, as subsequent events may be missed. Importantly, to be considered an event in the GeoNet catalogue, this automated process must detect picks on at least 10 stations (GeoNet, n.d.). This is almost certainly a limitation in capturing the full extent of microseismicity in the AVF, given that there are only 12 stations within the AVSN (Table 1).

3.4.2 Manual picking

A manual review of automated picks on unfiltered waveforms is the gold standard for seismic phase arrival picking. It is something that GeoNet has done often, occurring in 76 of the 91 events. However, with picks differing from reviewer to reviewer and multiple seismologists creating picks within this catalogue, the data will have consequential accumulated inconsistencies. Superimposed on the low-magnitude seismicity of the AVF, which already culminates in uncertain arrival picking through a reduced SNR, particularly for S-waves, which may have their initial energy concealed by that of prior phases, this user-dependent picking further amplifies the ambiguity of event locating.

To minimise these errors, many P -and S-wave picks are optimal for each event. Thus, with 15 events still to be reviewed, and due to several different reviewers making picks across the other 76 events, this study prioritized analysing the waveform data on each stream for each event in the catalogue, creating picks where there is high confidence. A bandpass filter was applied for stations where picks could not be made. Such a filter is accessed through the ObsPy package and applied in the frequency domain, removing all wavelengths from each stream signal outside of a user-defined passband, which was found by trial and error following the plotting of waveform data. Not only was the bandpass filter assigned to increase the SNR to a point where further picks were possible, but it also removed low-frequency signals, such as ground roll, for more aesthetic waveform plotting.

Due to this picking being a laborious task, with a best-case scenario capable of 2730 combined P-and S-wave picks, a Python code was developed for computational assistance (Appendix A). As alluded to in comments within this code, it iterates over each station for each of the 91 events by descending magnitude. Using the Matplotlib library, which produces interactive figures in Python, high-resolution P -and S-wave picks could be made utilising the zoom functionality (Hunter, 2007). Following observation of the complete waveform and visualisation of potential P -and S-wave arrival times, the code allows the user to first zoom into the P-wave arrival to make a pick by double-clicking and zoom out to the original view to then repeat the process for making the S-wave pick. For each station, the maximum number of picks possible before the window closes and the following stations waveform data appears is two, with the first and second picks respectfully

assigned to the P-wave and S-wave arrivals and saved in a .obs file for use in NonLinLoc. Here, the double-click function inhibits false arrivals from being made during the zooming process. After all stations have been iterated over for each event, a single .obs file with correctly assigned arrivals is made and stored in the user-defined directory.

In this study, such files were saved using the events GeoNet ID so that any misinterpreted "events" could be easily identified and rejected by GeoNet and also for comparison purposes. Where no picks or where only P-wave arrivals could be identified, the code successfully moved to the next station after manually closing the pop-up window. Although this hindered S-wave picks from being assigned without a P-wave pick first, such occurrences were unlikely given the low SNR these waveforms possess.

When manually picking P- and S-wave arrivals, consideration was made about their respective uncertainties. Although picks were only made where there was relatively high confidence, error is inevitable due to seismic waveform data embodying the superposition of signals of varying frequencies. Furthermore, Zeiler and Velasco (2009) showed that even a single manual analyst has variable picking times when presented with the same data on different occasions, with the SNR being the leading cause of error. For this study, assigning individual pick uncertainties at the time of picking was unfeasible, as this would disturb the iterative process enabled by the code in Appendix A. Thus, P- and S-wave picks were respectfully assigned uncertainties of ± 0.02 s and ± 0.05 s. A simple Python code completed this assignment, with the column to the right of GAU in the .obs files replaced by 0.02 s for P-waves picks or 0.05 s for S-waves picks.

3.5   NonLinLoc location methodology

All seismic events, constituting earthquakes and quarry blasts, were relocated using NonLinLoc (Lomax et al., 2000). As the name suggests, this programme is a non-linear event relocation algorithm, following the probabilistic inversion and location approach of Tarantola (1987) and Tarantola and Valette (1982), in addition to other location methods of Moser et al. (1992) and Wittlinger et al. (1993). Four critical constituents of this programme are outlined below: the input control file, the inversion problem, the data misfit, and the model null space.

3.5.1 Input control file

NonLinLoc's package control file contains all relevant information on the requirements for event location using this software. Statements are assigned priorities of "required," "optional," "repeatable," and "ignored," with those labelled as "required" necessary for any outputs to be obtained. Within this control file, alongside Generic Control Statements, three essential programmes, Vel2Grid, Grid2Time, and NLLoc, are utilised. The complete control file used in this study is given in Appendix B. However, the general workflow and main requirements of these four controls are defined below.

1. Generic Control Statements: In the Generic Control Statements, a geographic transformation statement, TRANS, is defined. For the AVF, the Transverse Mercator projection was used alongside the GRS80 reference ellipsoid for consistency with Land Information New Zealand (Toitū Te Whenua Land Information New Zealand, n.d.). However, the origin latitude and central meridian were adapted to coincide with the AVF (Appendix B).

2. Vel2Grid: Within the Vel2Grid programme, requirements include an output velocity model directory accessed through the VGOUT statement, a VGGRID velocity grid description specifying the grid size and dimension, and, finally, the velocity model, which includes the subsurface layers, and their respective depths and P- and S-wave velocities. With this, the Vel2Grid command defines each model's phase velocities at each grid point.

3. Grid2Time: The Grid2Time programme takes the velocity grid previously generated using the Vel2Grid command and calculates travel times for the defined seismic phases from each grid point to each station. It is best to include the station ".txt" file within this control file with additional GTSRC statements (Table 1). Notably, despite picks being made on stations TOZ, GRZ, and KUZ, only stations within the AVSN were used in this study. Through GTFILES statements, both P-and S-wave travel-time grids are output, although these must be run separately by manually commenting out one phase and then the other. This is crucial to the uncertainty of any event locations obtained, as having just the S-wave travel-time grid, which is the default, means that only S-wave arrivals within the .obs files can be run through the model, as seen with the NLLoc programme.

4. NLLoc: The NLLoc programme, including an array of "required" statements, takes the .obs files passed to the programme through a LOCFILES statement, runs these through the previously engineered time grid from the Grid2Time command, and outputs the most probable hypocentre attributes of these events, including their locations and any residuals. Within this programme, LOCGRID, describing the location search volume, must be large enough to contain the target seismicity. The LOCMETH command defines the method parameters and the location method algorithm and includes a V_p/V_s ratio. For both P-and S-wave travel-time grids to be read, this ratio must be negative and has been suggested by A. Lomax (personal communication, August 11, 2023), to be -9.99 for clarity. This is because NLLoc uses separate V_p and V_s models when V_p/V_s is negative, but when V_p/V_s is positive, it only utilises the S-wave model and picks when P-wave travel-times are unavailable for a given station.

3.5.2 Inversion problem

The inverse problem is described by Snieder and van Wijk (2015) as one where wave observations are made before trying to interpret the internal structure of the medium producing these data. This relationship comes from the matrix equation **d = Am**, perfectly encapsulating what creating a velocity model for seismological investigation is. Here, the data vector, **d**, embodies the P-and S-wave phase arrival times, while the forward operator, **A**, the physics of the problem, and the velocity model, **m**, combine to form the predicted phase arrivals **Am**. As such, the inverse problem is to adjust the velocity model parameters until the predicted data approaches the real data. More simply, this is to minimise $\|\mathbf{Am - d}\|^2$.

However, within this inversion, the NonLinLoc algorithms used to obtain predicted travel times and hypocentre locations, Grid2Time and NLLoc, respectively, constitute forward problems in their own right (Lomax et al., 2000).

Three primary methods are considered for travel-time calculations: full-waveform methods, ray methods, and Eikonal, or Huygens wavefront methods (Lomax et al., 2009). Of these, NonLinLoc employs the Eikonal finite-difference approach of Podvin and Lecomte (1991), representing the repeated application of Huygens principle (Huygens, 1690). This principle originates from optics, depicting wave propagation as a superposition of spherical wavelets emanating from each point

on a wavefront. The Eikonal equation, on the other hand, comes from the geometric ray theory approximation, embodying a particular case of Huygens principle arising under scenarios where the length scales of the propagating medium are much greater than the wavelength (Equation 7) (e.g., Snieder and van Wijk, 2015). Resultantly, the Eikonal equation is merely a simplification of the wave equation under high-frequency scenarios (Equation 1). Here, wave propagation is described by rays travelling normal to planar wavefronts, with the gradient of the wave's travel time from the source to a point in space, $\nabla T(\mathbf{r})$, depending on the local medium velocity, $v(\mathbf{r})$.

$$|\nabla T(\mathbf{r})|^2 = \frac{1}{v(\mathbf{r})^2} \tag{7}$$

For this forward problem, predicted P-wave arrivals for each station are, therefore, found by solving the numerical solution to the Eikonal equation; however, S-wave arrivals require more complex multi-stage calculations (Lomax et al., 2009; Podvin and Lecomte, 1991). Unlike geometric ray theory, this algorithm within Grid2Time considers caustics induced by velocity contrasts, with travel-time gradient discontinuities constructed as intersections of independent wavefronts (Lomax et al., 2000).

For hypocentre locating, a Bayesian framework was implemented, which describes the probability of determining the source location parameters, $\mathbf{m}$, given some data, $\mathbf{d}$ (Lomax et al., 2009). Bayes' Theorem defines this relationship (Equation 8).

$$p(\mathbf{m}|\mathbf{d}) \propto p(\mathbf{d}|\mathbf{m})p(\mathbf{m}) \tag{8}$$

This solution is illustrated in terms of probabilistic density functions (*pdf*'s). Here, $p(\mathbf{d})$ and $p(\mathbf{m})$ respectively represent the *pdf* of uncertainty in the observed arrival times, and the prior *pdf* without any knowledge of the data, $\mathbf{d}$. The prior is influenced by the likelihood function, $p(\mathbf{d}|\mathbf{m})$, outputting the posterior probability function, $p(\mathbf{m}|\mathbf{d})$. The approach of Tarantola (1987) and Tarantola and Valette (1982) uses this framework to obtain a posterior *pdf* and, in turn, evaluate the probabilistic hypocentre location for each event.

3.5.3 Data misfit

The Equal Differential Time (EDT) likelihood function was used in this investigation to assess the misfit: how well the model, **m**, explained the observed data, **d** (Font et al., 2004; Lomax, 2005; Zhou, 1994). This function assumes that observation errors are Gaussian, simplifying the location problem from 4D to 3D due to no origin-time dependence (Lomax et al., 2000). This 3D grid search over latitude, longitude, and depth occurs alongside importance-sampling, with the Oct-tree method utilised (Lomax and Curtis, 2001). Oct-tree generates a cascade of sampled cells from the location *pdf*, with the hypocentral uncertainty displayed in scatter form (Figure 2). This study did not incorporate such a visualisation; however, it illustrates how the maximum likelihood hypocentre represents the point in the location *pdf* where the misfit is minimal and the concentration of Oct-tree samples is highest.
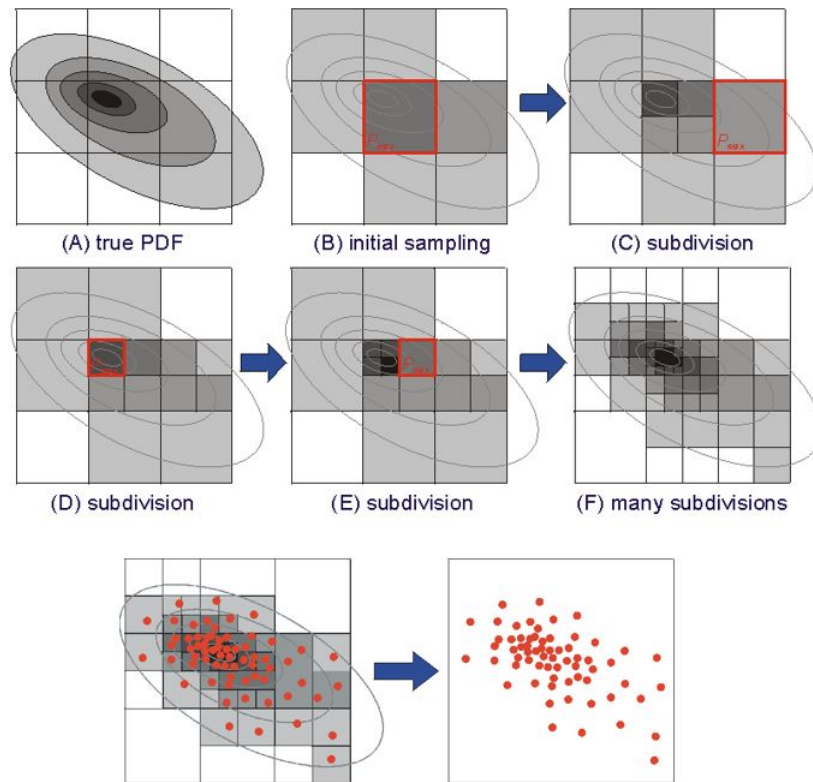
Figure 2: Oct-tree sampling algorithm of Lomax & Curtis (2001). From the true probability density function (*pdf*) for a given event, Oct-tree generates a cascade of sampled cells. The maximum likelihood hypocentre is the point where the misfit is minimal and the concentration of Oct-tree scatter points is greatest.

Mathematically, the misfit signifies the difference between the observed and predicted arrivals, T_{obs} and T_{pred}, respectively. These residuals, Res, are calculated for each event for both P- and S-phases at each station. Within the output hypocentre files, Res>0 and Res<0, respectively, imply that predicted arrivals are arriving faster and slower than the real observations.

The hypocentre file output by NonLinLoc provides further location quality metrics, such as the weighted root-mean-square (RMS) of arrival residuals and the spatial characteristics of the confidence ellipsoid. Such data are used in this investigation to interpret the quality of individual events within different trialled models alongside their average performance relative to those produced by GeoNet.

3.5.4   Null space

Although location quality metrics inform the likelihood of **m** producing the measurable quantities of **d** and **A**, model gridpoints can remain unsampled by seismic rays during relocation, embodying components of the model null space (e.g., Snieder and van Wijk, 2015). Several factors influence the model null space and, therefore, the volume of gridpoints insensitive to the data misfit. Some examples are the dispersion and number of seismometers in the AVSN and the source location. However, with the AVSN distribution being pre-determined, interpreting the most representative model using misfit, in turn, relies on the model's training using scattered source locations (Section 3.6.2).

3.6   Velocity models

3.6.1   iasp91 Model

The performance of the iasp91 model, published by Kennett and Engdahl (1991), was evaluated in this study, having been the primary velocity model used by GeoNet since 2018 (GeoNet, 2022. Although this model provides velocities for the entire cross-section of Earth, the uppermost 35 km is utilised here (Table 2). With seismicity in the AVF generally nucleating shallower than 15 km, 35 km depth is likely sufficient in capturing the extent of the seismogenic zone (Deligne et al., 2019).

Table 2: Simplified V_p and V_s with depth for the iasp91 model (Kennett and Engdahl, 1991). Positive depth values indicate land below mean sea level).

Depth (km)	$V_p \left(\frac{\text{km}}{\text{s}} \right)$	$\frac{V_p}{\text{km}} \left(\frac{\frac{\text{km}}{\text{s}}}{\text{km}} \right)$	$V_s \left(\frac{\text{km}}{\text{s}} \right)$	$\frac{V_s}{\text{km}} \left(\frac{\frac{\text{km}}{\text{s}}}{\text{km}} \right)$
-1	5.8	0	3.36	0
20	6.5	0	3.75	0
35	8.04	0	4.47	0

3.6.2 Homogeneous model

The simplest model possible to represent any subsurface is one that is isotropic, where rock properties, and consequently P-and S-wave velocity values described through Equations 5 and 6, are spatially and temporally homogeneous. Although such simplifications are never accurate in the real world due to subsurface heterogeneities and anisotropy, which influence directional velocity within the seismogenic crust, a homogeneous model provides the first step in recognising any regional complexities and trends that could be modelled. Occam's razor underpins this principle, suggesting that the exploration of complex models is only justified when supported by the results of the simplest case.

NonLinLoc was used to calibrate this homogeneous model, where the "best" model was aimed to represent that with the lowest average RMS misfit. To do this, the training, test, and validate split was implemented, with 70% of the catalogue placed into training data, 20% into test, and 10% into validation, utilising the 'os,' 'shutil,' and 'random' Python modules. For any real-world system where modelling is undertaken, such a split is favourable as it eliminates the bias of training a model on the "best" data, which is unrepresentative of the whole catalogue. The AVF is no different in this respect, with anthropogenic noise and picking uncertainties going to be continuously unavoidable. Thus, instead of training a model on selected, perhaps larger magnitude events that are predetermined to have both P-and S-wave picks on most stations, this random selection not only attempted to minimise the model null space but ensured that the analysis was not overly perfect. Theoretically, these considerations increase the resultant model's utility in locating future or previous seismic events outside this original catalogue.

To get a starting point for the most probable V_p and V_s to optimise around, a comparison was

initially made with previous models, such as the iasp91 model, and that produced by Barter (2021), which indicate likely values of around V_p = 6 km/s and V_s = 3.5 km/s for the uppermost 20 km of crust. Comparatively, over the 44 km crustal depth in the Ashenden et al. (2011) model, a similar average for V_p is suggested for the AVF. From this, V_p was chosen to be optimised first, involving perturbation to 5, 5.5, 6, 6.5, and 7 km/s for a constant V_s, with various values of V_s = 2.5, 3, 3.5, 4, and 4.5 km/s independently tested. The training and test datasets were run through these 25 models, from which their respective average RMS residuals were plotted to gauge the V_p with the lowest uncertainty. Furthermore, in observing the V_s value producing this optimised V_p, V_s was then able to be optimised by perturbing to $\pm$ 1 km/s of this value, in 0.5 km/s increments. This process also involved the training and test datasets, instead this time with V_p held constant. The validation data was then run through these velocity models that optimised V_p and V_s. Comparisons between the optimum V_p and V_s values producing the lowest average RMSs were vital in interpreting the model's validity and justifying the "best" homogeneous case to run the entire catalogue through for event locating.

4 Results

4.1 Arrival Picking

Of the 91 events within GeoNets catalogue, 86 were considered real sources of seismicity, with 2012p710024, 2013p499253, 2014p542288, 2015p123092, and 2023p164059 rejected. With a small proportion of this catalogue yet to be manually reviewed by GeoNet, most events should have relatively accurate picks approximating those made in this study. Figure 3 delineates this for event 2013p203042. At first glance, there is an agreement between these two datasets, particularly for each stream's first arrival, which results from the higher SNR. Although picking subsequent phase arrivals has more significant ambiguity, GeoNet appears to have missed some S-wave arrivals for this M3.2 event, an observation discernible across the entire catalogue, even with manual review.

Despite the correlation with GeoNet's P-wave picks being demonstrated, zooming into the station streams highlights how, even with the manual review, their first arrivals generally represent the peak of the first wavelength on the unfiltered waveform rather than the initial onset of seismic
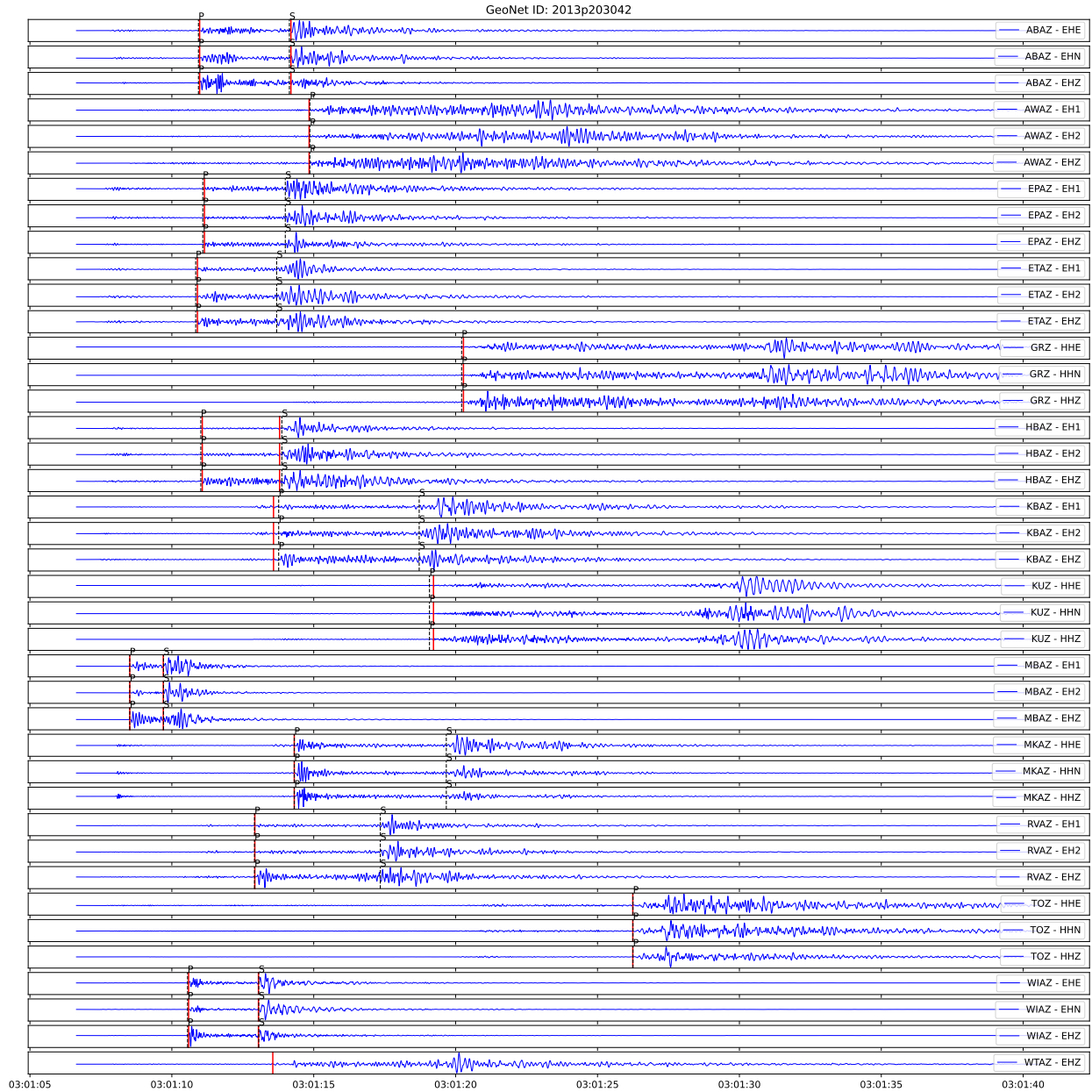
Figure 3: Plot of earthquake 2013p203042 waveform data with GeoNet's P -and S-wave arrival picks given in red, and those of this study in black.

energy (Figure 4). This is likely a consequence of not zooming in far enough to check the STA/LTA automated picks; however, it is significant as the combination of higher resolution P-wave picks and additional S-wave picks is likely to produce more reliable source locations in a given velocity model.

Although most picks were made on unfiltered data, all plots like Figure 3 embody the filtered

20

waveforms for aesthetic purposes. A bandpass filter with no phase shift was applied, with frequencies <5 Hz and >20 Hz effectively removed. Additionally, cosine tapering occurred to remove artifacts near the edge of each stream window, with a maximum percentage of 0.05 Hz used. For further afield stations such as GRZ, KUZ, and TOZ, several P-wave arrivals were picked on these filtered traces, given the long wavelength ground roll removal. However, assessing whether these changes shifted these first arrivals is essential. Figures 4 and 5 demonstrate little change in the onset of P-wave energy; thus, these picks made on filtered traces are taken as representative of the actual arrivals. Although picks on these three stations were not used in this investigation, such a result foreshadows their utility in future work.
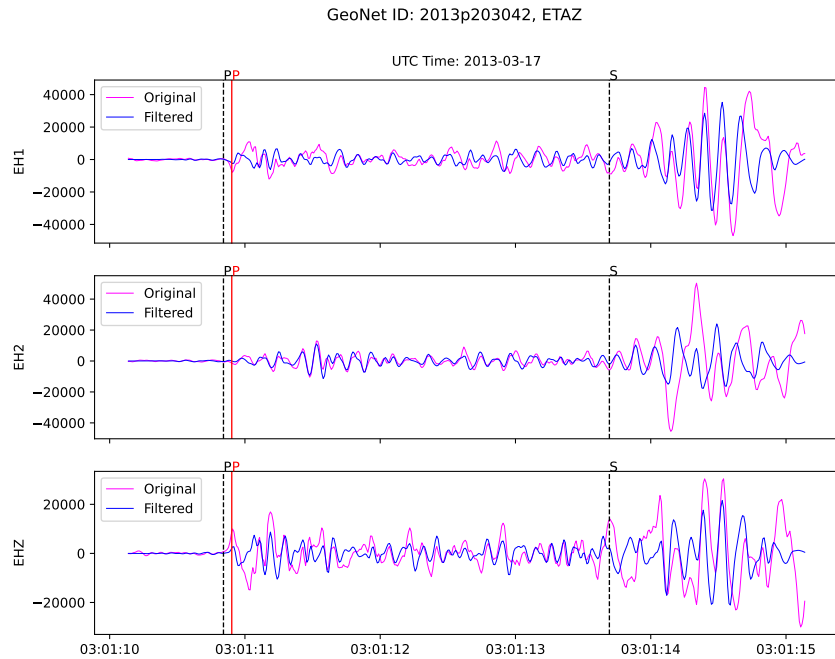
Figure 4: Plot of earthquake 2013p203042 unfiltered (magenta), and filtered (blue) waveform data on station ETAZ. GeoNet's P -and S-wave arrival picks given in red, and those of this study in black.

4.2   Homogeneous model

Training of the V_p model, while V_s was perturbed, demonstrates a clear trend that as V_s increases, the V_p value representing the local minima, or lowest RMS of each fitted parabolic curve increases (Figure 6). For instance, $V_s = 2.5$ km/s produces a minimum RMS of 0.26 s at $V_p = 5.57$ km/s, while $V_s = 4.5$ km/s produces that of 0.26 s at $V_p = 6.90$ km/s, with good correlation for each curve
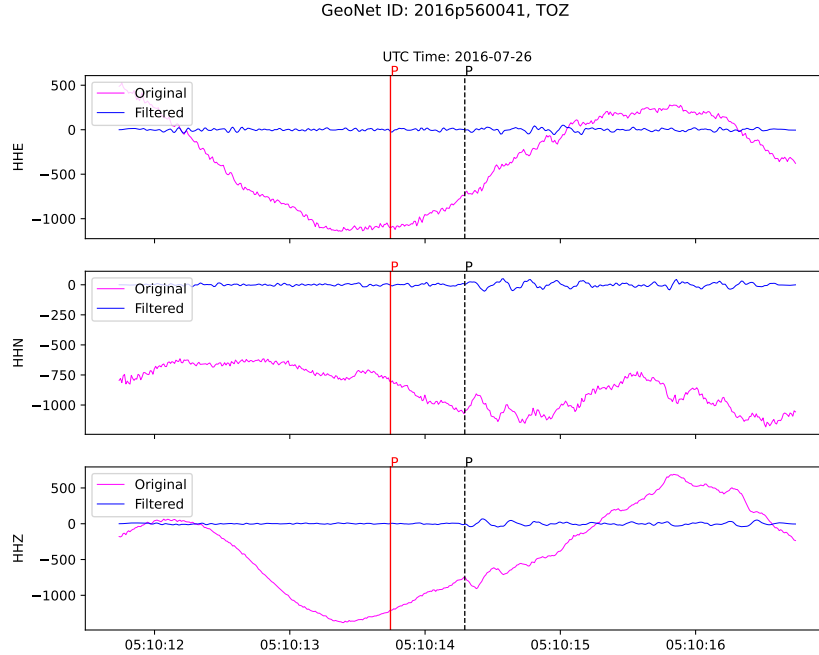
Figure 5: Plot of earthquake 2016p560041 unfiltered (magenta), and filtered (blue) waveform data on station TOZ. GeoNet's P -and S-wave arrival picks are given in red, and those of this study in black.

evident after overlaying the test dataset results. These two V_s end-members produced the largest RMS residuals, with the smallest RMS local minima of 0.14 s and 0.13 s, coinciding with $V_s = 3$ km/s and $V_s = 3.5$ km/s, respectively. Although it is not shown in (Figure 6), $V_s = 3$ km/s was also trialled with $V_p = 4.5$ km/s to constrain further the local minima provided from this model given how similar the RMS is with that of $V_s = 3.5$ km/s. However, the position and RMS of this minima did not change, indicating that $V_s = 3.5$ km/s produced an optimised $V_p = 5.94$ km/s with RMS = 0.13 s, approximately coincident with values produced by the test dataset.

Using this verified V_p of 5.94 km/s, the training dataset indicates an optimised V_s value of 3.39 km/s, with RMS = 0.15 s, with results obtained by the test dataset approximately conforming (Figure 7). Results from running the 10% validation dataset through these optimised V_p and V_s models show a more significant increase in the minimum RMS values relative to the increase between the training and test sets, with 0.17 s and 0.16 s, respectively. Furthermore, for this validation dataset, the refined V_p value increases to 6.43 km/s, while that of the V_s decreases to 3.14 km/s; however, with just 10% of the catalogue within this set, such shifts are expected as theoretically, these events could have been randomly selected as some with the smallest magnitudes

22

and the least picks made. Therefore, the implementation of training, testing, and validating the homogeneous model suggests that optimised velocities for the AVF subsurface are V_p = 5.94 km/s and V_s = 3.39 km/s (Table 3).
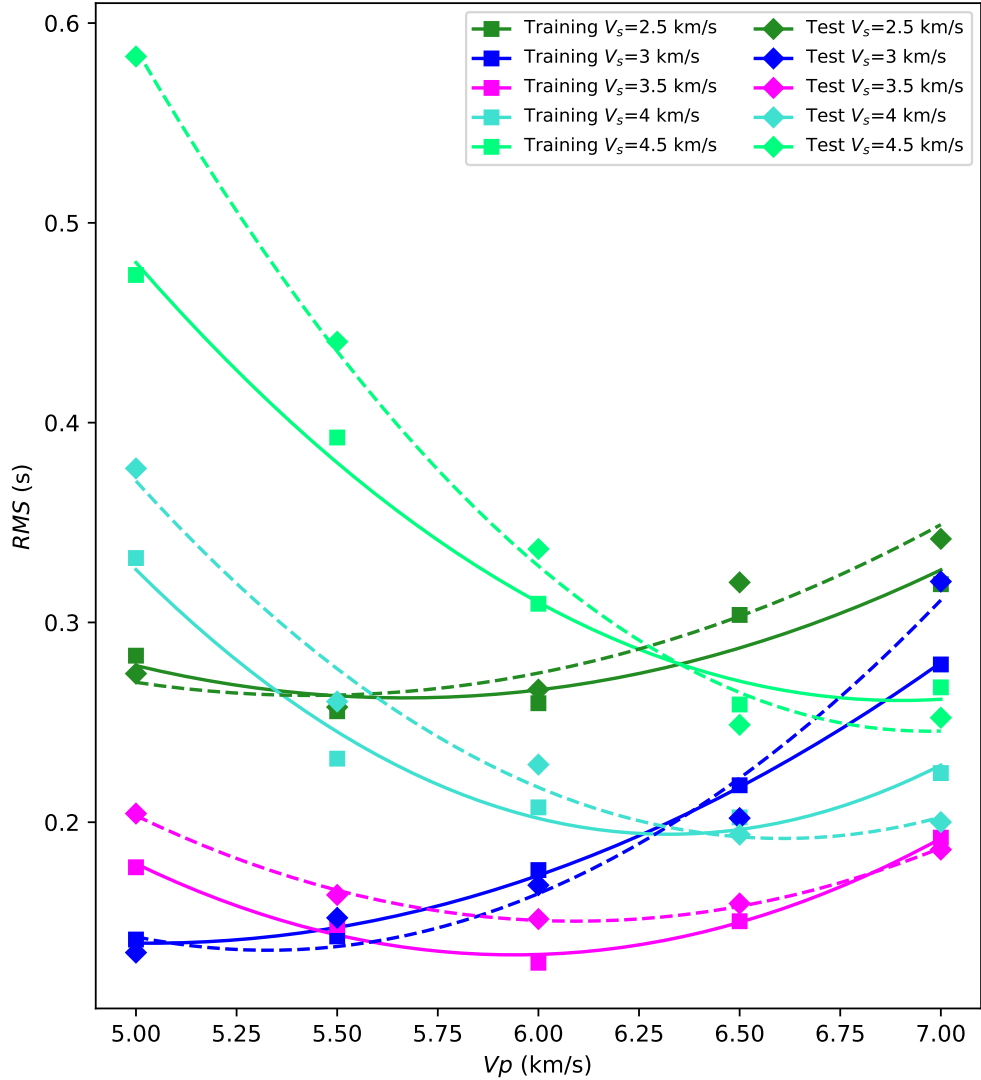
Figure 6: Plot of V_p calibration where V_p has been perturbed to 5, 5.5, 6, 6.5, and 7 km/s while V_s has been kept constant at 2.5, 3, 3.5, 4, and 4.5 km/s, respectively. Squares and solid lines are results from the training data, while diamonds and dashed lines are results from the test data. The lowest average RMS occurs for V_s = 3.5 km/s with a local minimum at V_p = 5.94 km/s after plotting a parabolic fit.
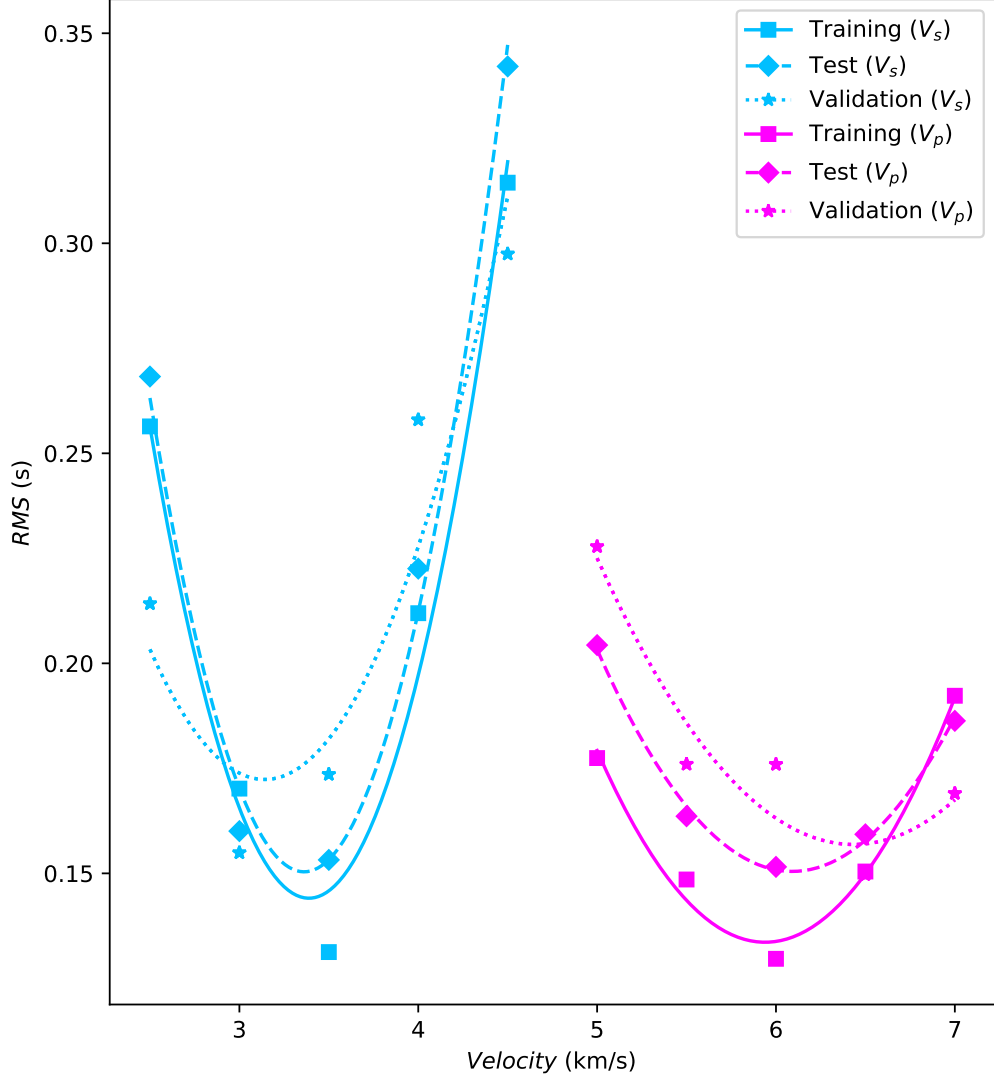
Figure 7: Plot of results from the V_s optimisation through perturbing this value to 2.5, 3, 3.5, 4, and 4.5 km/s while keeping a constant V_p of 5.94 km/s. Alongside this are the results from the V_p calibration with validation data overlain on both. Squares and solid lines are results from the training data, diamonds and dashed lines are results from the test data, and stars and dotted lines are results from the validation data. The lowest average RMS for V_s occurs at a local minimum of 3.39 km/s in the training dataset following plotting of a parabolic fit.

Table 3: Optimal V_p and V_s for a homogeneous model of the AVF. Values are derived from running the catalogue of events, which was split into the training, test, and validation ratio (70:20:10), through a systematic optimisation process in NonLinLoc.

Depth (km)	$V_p \left(\frac{\text{km}}{\text{s}}\right)$	$\frac{V_p}{\text{km}} \left(\frac{\frac{\text{km}}{\text{s}}}{\text{km}}\right)$	$V_s \left(\frac{\text{km}}{\text{s}}\right)$	$\frac{V_s}{\text{km}} \left(\frac{\frac{\text{km}}{\text{s}}}{\text{km}}\right)$
-1	5.94	0	3.39	0

4.3 Comparison of models

4.3.1 iasp91 and Homogeneous

Running the 86 events through the iasp91 and homogeneous models in NonLinLoc produced comparable event locations and RMS values (Figure 8). Furthermore, the average RMSs of these models approximate one another at 0.115 ± 0.06 s and 0.118 ± 0.06 s, respectively (Table 4). To 20 km depth, iasp91 has $V_p = 5.8$ km/s, and $V_s = 3.36$ km/s (Table 2). With optimisation of the homogeneous model producing V_p and V_s of 5.94 km/s and 3.39 km/s, respectively, this suggests that small variations in phase speeds on the order of 10^{-1} km/s do not significantly change attributes of the most probable event locations. With the RMS values being so similar, the homogeneous model of this study is used to compare with GeoNet event locations.
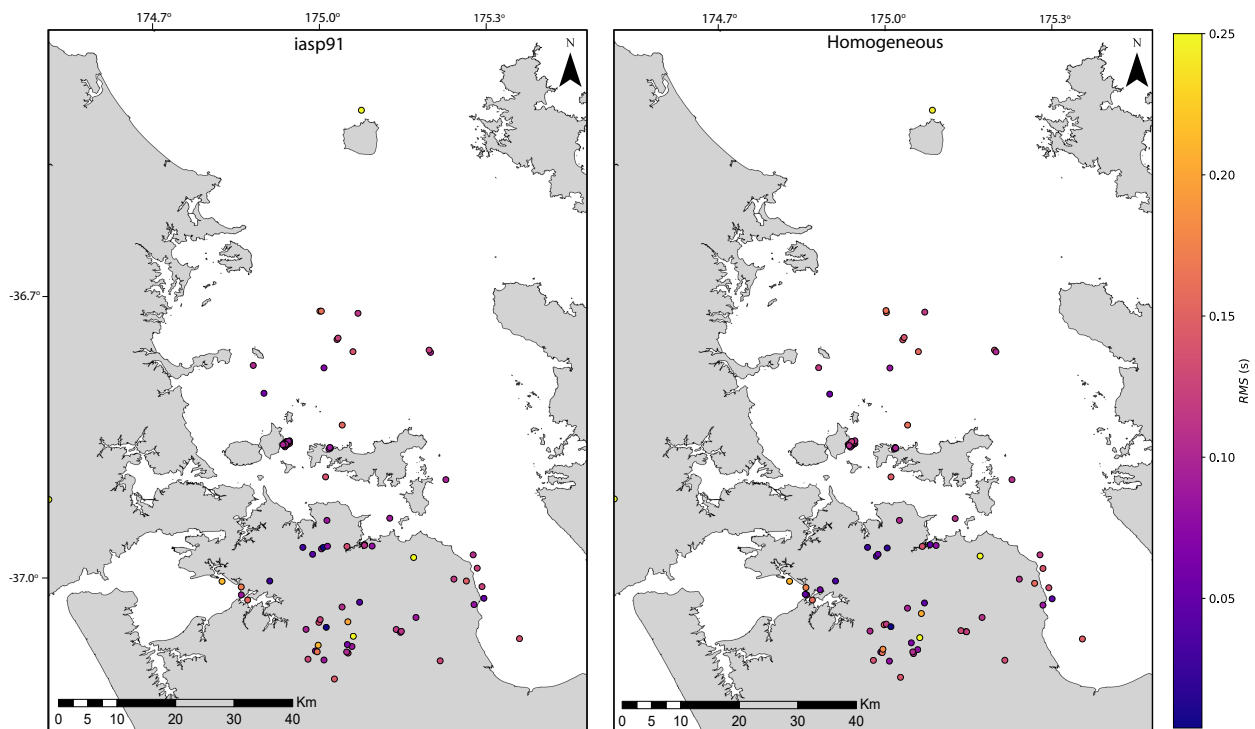
Figure 8: Map of Auckland comparing the iasp91 (left) and homogeneous model (right) event locations, and RMS values. Both models locate earthquakes in approximately the same place, with comparable RMS.

Table 4: Average RMS and standard deviation for the iasp91 model, homogeneous model, and GeoNet locations. Iasp91 and homogeneous values are obtained from running the 86 events through NonLinLoc, while those of GeoNet are from within their catalogue, for the same events.

Model	Avg. RMS (s)
iasp91	0.115 ± 0.06
Homogeneous	0.118 ± 0.06
GeoNet	0.403 ± 0.3

4.3.2 GeoNet and Homogeneous

Relative to the GeoNet event locations, those produced using the homogeneous model demonstrate significant variability, with virtually no one event placed at the same horizontal geographic position (Figure 9). Although there is better agreement concerning hypocentre depths, those from this study reside at an average depth of 8.0 ± 5 km, deeper than GeoNet at 6.0 ± 4 km (Figure 9). However, with 14 of the 86 events in GeoNets database being allocated as quarry blasts with "operator assigned" depths of 0 km, it is difficult to compare the two. Furthermore, plotting a rose diagram of the plunge from horizontal of all confidence ellipsoid semi-major axes depicts a mean resultant direction of 091°- 271°, emphasising that the most significant location uncertainty is in the z-direction (Figure 10). With this, the focus of comparison is, therefore, the 2D geographic locations.

The average RMS of GeoNet locations and those from the homogeneous model are 0.403 ± 0.3 s and 0.118 ± 0.06 s, respectively. Figure 11 portrays this remarkable reduction in RMS, evident across virtually all events in the catalogue. Also seen in Figures 9, 11 and 12 is the homogeneous model and updated picks resulting in an offshore cluster of 19 earthquakes east of Motutapu Island, all residing within 7.2-8.4 km from the surface. Contrastingly, GeoNet locates these same events at variable locations proximal to Rangitoto Volcano and Motutapu Island, with depths equally inconsistent at 4.1 - 9.6 km. Although these updated locations have an average confidence ellipsoid semi-major axis half length of 0.94 ± 0.3 km, their mean resultant plunge direction is vertical, at 094°- 274°(Figure 13). Without even accounting for the uncertainty of GeoNet event locations, which are likely higher given their larger RMS, the cluster produced from the homogeneous model relocation gives a better-constrained depth extent.
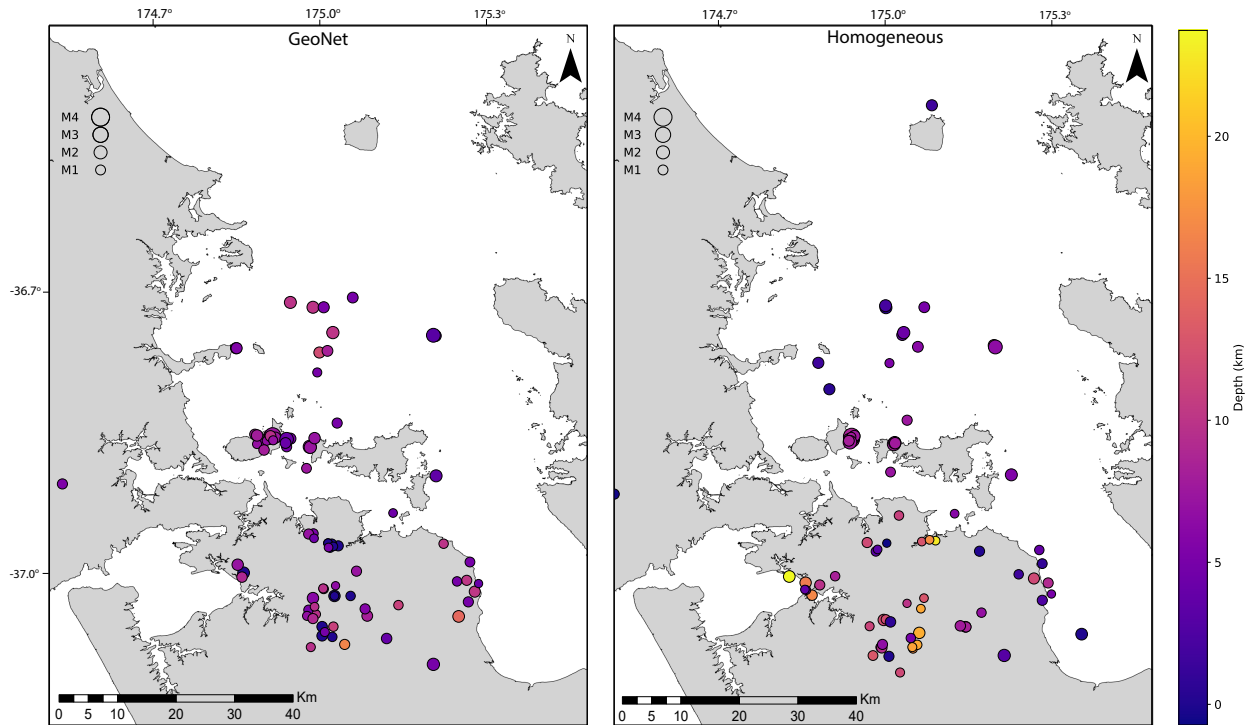
Figure 9: Map of Auckland comparing the Geonet (left) and homogeneous model (right) event locations, and depth values. The circle size represents the GeoNet assigned magnitude.
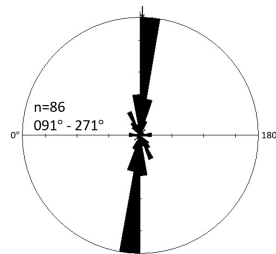
Figure 10: Rose diagram of the plunge from horizontal of all confidence ellipsoid semi-major axes for the homogeneous model. The mean resultant direction is 091°- 271°, showing that hypocentre depth is the largest uncertainty.

Although these events cluster in space, they do not all cluster in time, with isolated events nucleating throughout 2012, 2014, and 2016 (Figure 14). Contrastingly, after events 2013p203042 (M3.2) and 2013p203051 (M4), occurring at 2013-03-17T03:01:05 and 2013-03-17T03:05:42, respectively, ten events followed, ending just over a month later at 2013-04-20T06:34:27.
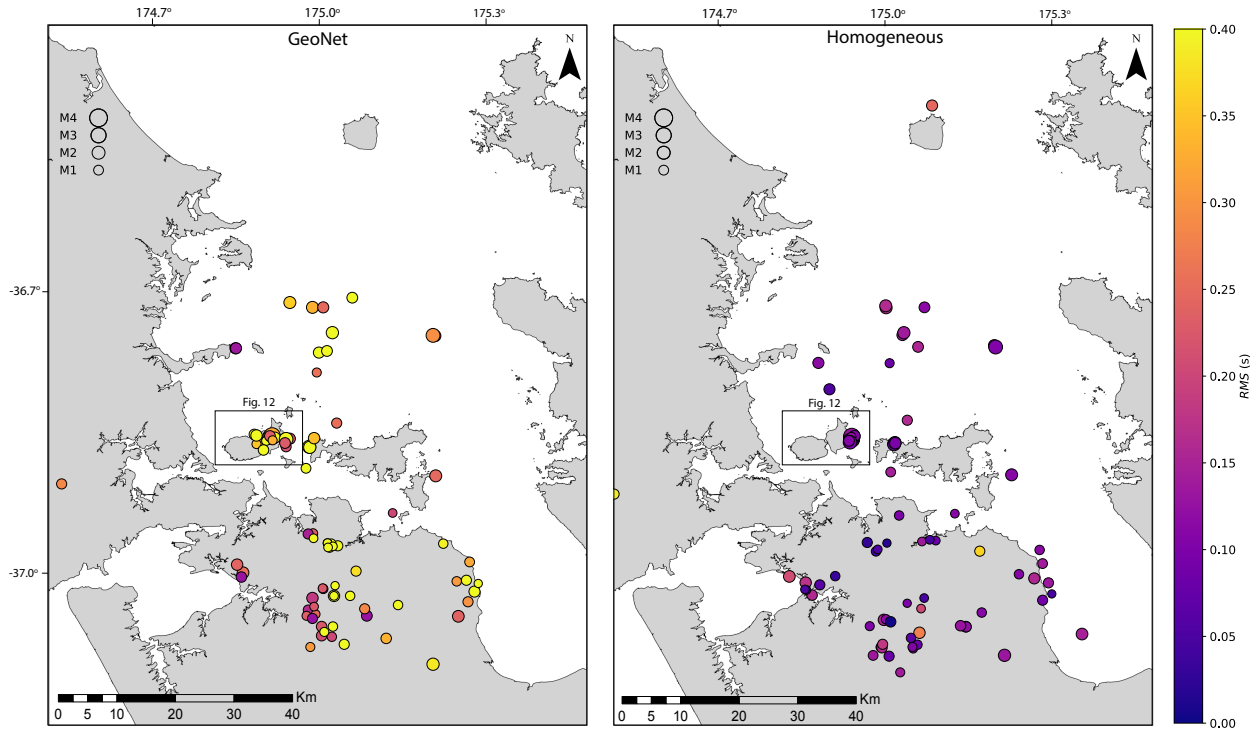
Figure 11: Map of Auckland comparing the GeoNet (left) and homogeneous model (right) event locations, and RMS values. The circle size represents the GeoNet assigned magnitude. Locations are seen to be highly variable, with the RMS of GeoNet locations much greater than those of the homogeneous model. The colour bar has been cut-off at RMS = 0.40 s to better delineate the values for the homogeneous model at the lower end of the spectrum. However, the maximum RMS from GeoNet reaches 2.57 s. Also indicated is the location of Figure 12.
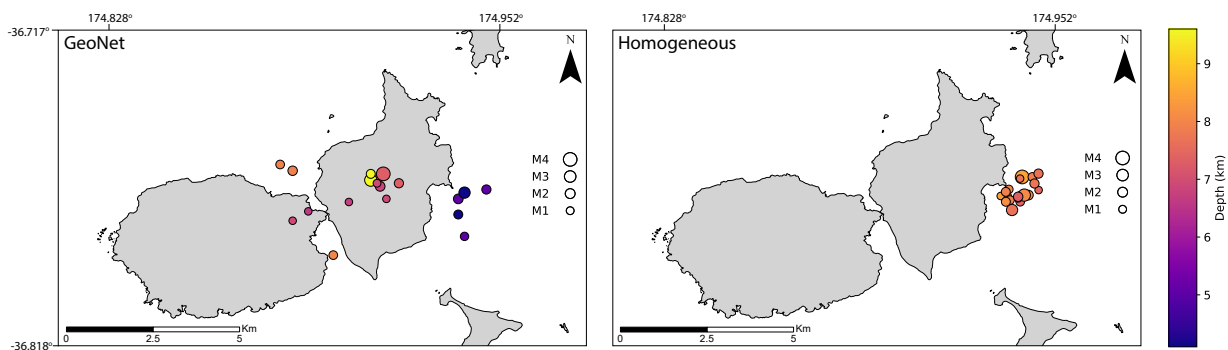
Figure 12: Spatial distribution of earthquakes proximal to Rangitoto volcanic island, comparing those from GeoNet (left), with those of this study using the homogeneous model (right). The homogeneous model, and updated picks locate the 19 earthquakes in an offshore cluster east of Motutapu Island, with depth ranging from 7.3-8.4 km. GeoNet's locations are spatially variable, with depth ranging from 4.1-9.6 km.
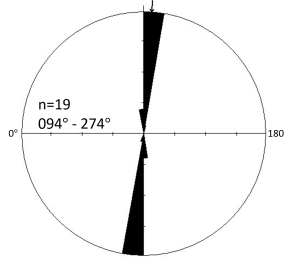
Figure 13: Rose diagram of the plunge from horizontal of confidence ellipsoid semi-major axes for the homogeneous model associated with the 19 events in the Rangitoto cluster. The mean resultant direction is 094°- 274°, showing that hypocentre depths is the largest uncertainty.
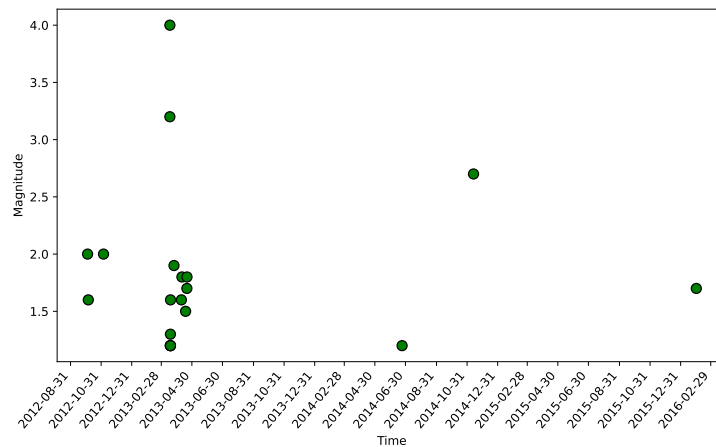
Figure 14: Plot of GeoNet-assigned magnitude as a function of time for the 19 events within the Rangitoto cluster. Events occurring in 2013 look to follow M3.2 and M4 earthquakes on 2013-03-17, while wider events spanning 2012, 2014 and 2016, seem discrete.

4.3.3 Quarry blasts: GeoNet and Homogeneous

Of the 86 events, 14 are unclassified by GeoNet, alongside 54 and 18 labelled as earthquakes and quarry blasts, respectively. All waveforms have been reviewed to complete the catalogue update, resulting in each of the 14 unknown events being reclassified as earthquakes, given their inherent P- and S-wave arrivals, similar to Figure 3. However, during this review, the distinctive waveform shape produced by quarry blasts became evident, a result equally apparent throughout the picking process (Figure 15). With such explosions generally lacking S-wave energy, events within Table 5 have been redefined as earthquakes, reducing the 18 quarry blasts within the catalogue to eight.

Figure 16 displays the spatial relationship of these reclassified events compared to GeoNet's. From this, one would assume that most of the 10 redefined events would be from within the south-
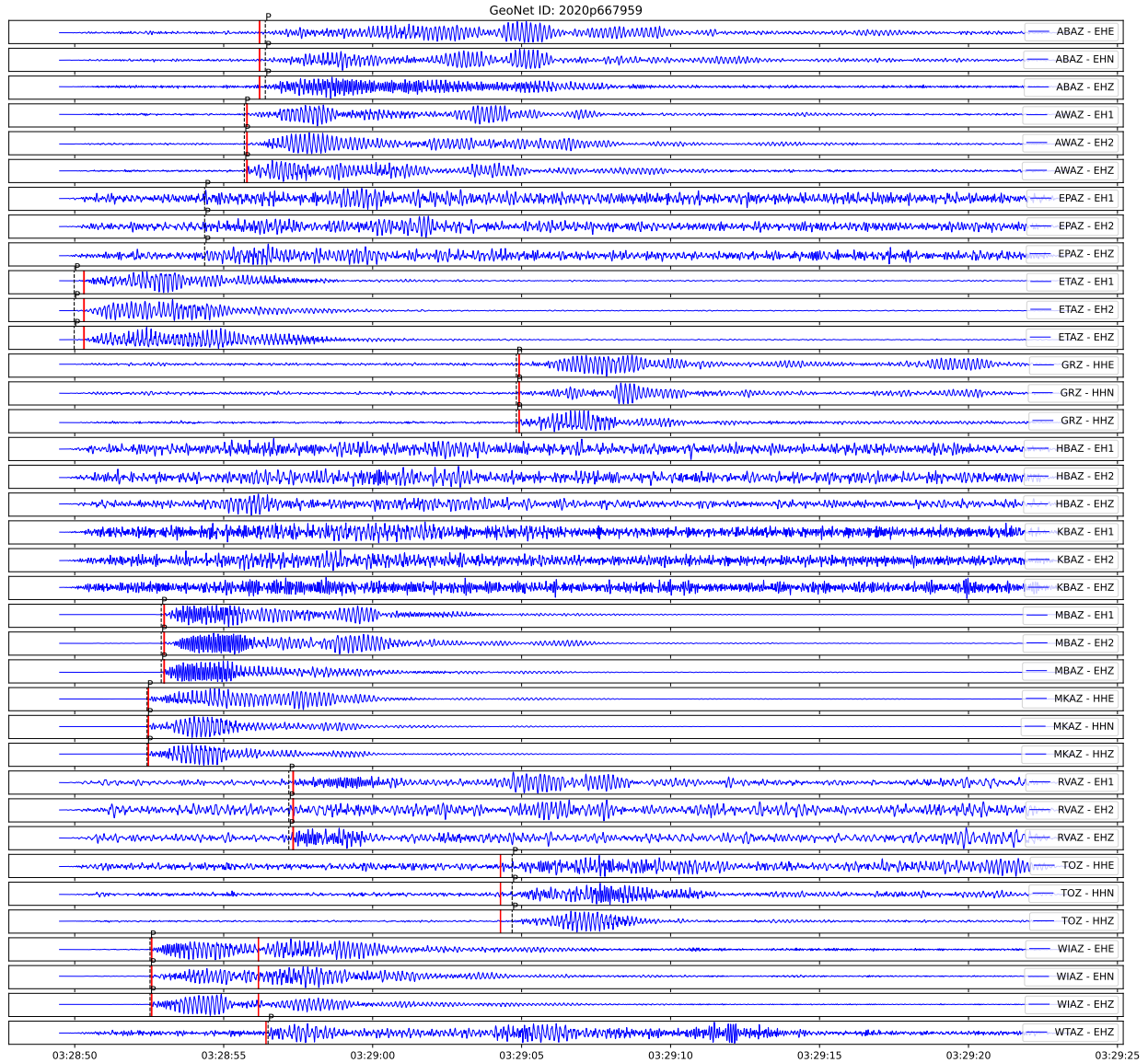
Figure 15: Plot of quarry blast 2020p667959 waveform data, with GeoNet's P -and S-wave arrival picks given in red, and those of this study in black. These explosive events generally lack S-wave energy and have a distinctive waveform morphology

ernmost quarries. However, as demonstrated, one of those eight quarry blasts resided within a southern quarry based on GeoNets modelling. This event, 2019p849100, has since been shifted in this study nearer to the northern quarries, demonstrating the potential impact an "operator assigned" depth of 0 km has on the event location. The further seven quarry blasts have been similarly relocated, with six of these assigned a depth of 0 km in GeoNet's catalogue.

Table 5: Events that have been classified by GeoNet as quarry blasts, but redefined here as earthquakes based on their waveform morphology.

GeoNet ID
2012p638181
2012p951489
2013p697341
2014p459683
2014p867461
2014p868169
2015p749091
2016p397465
2016p605416
2017p713388
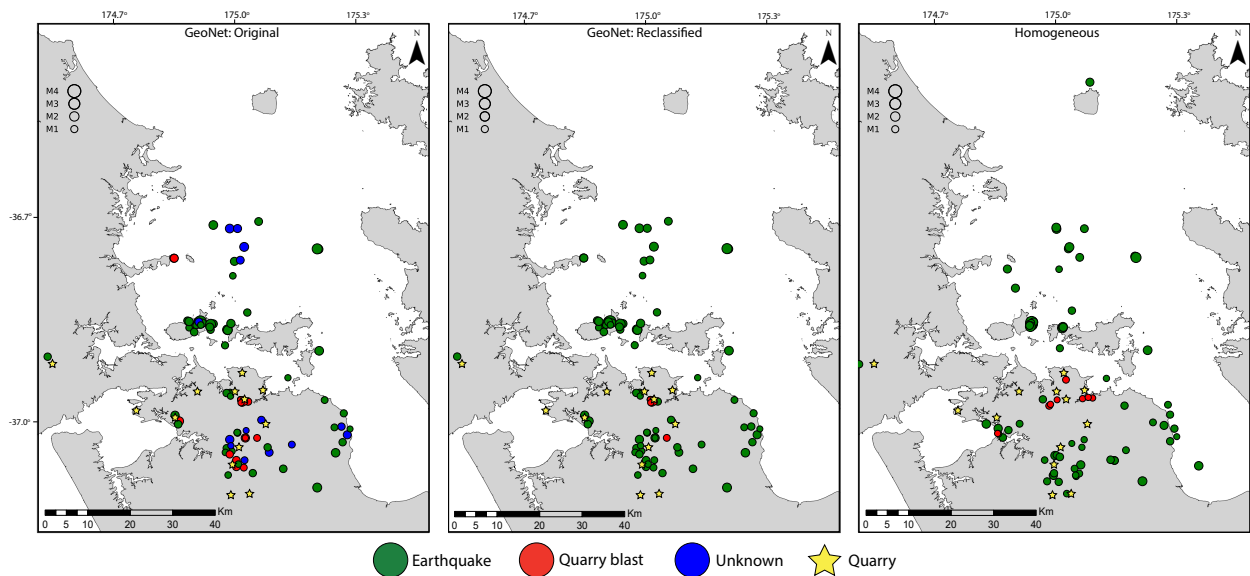
Figure 16: Map illustrating event location and type: earthquake (green), quarry blast (red), or unknown (blue). Original classifications from GeoNet are shown (left), alongside the reclassified dataset of GeoNet (middle), and the homogeneous model (right).

4.3.4 Mapped faults: GeoNet and Homogeneous

Comparing the GeoNet and homogeneous model event locations of redefined earthquakes with the Kenny et al. (2012) compilation of Post-Miocene faults provides another means of qualitatively interpreting the success of the relocation (Figure 17). Three primary regions of seismicity are evident within both location datasets: the eastern basement faults compiled by Edbrooke (2001), and the inferred faults of Kenny et al. (2012) within the Manurewa Horst, and the Hauraki Gulf,

including the previously defined Rangitoto cluster.
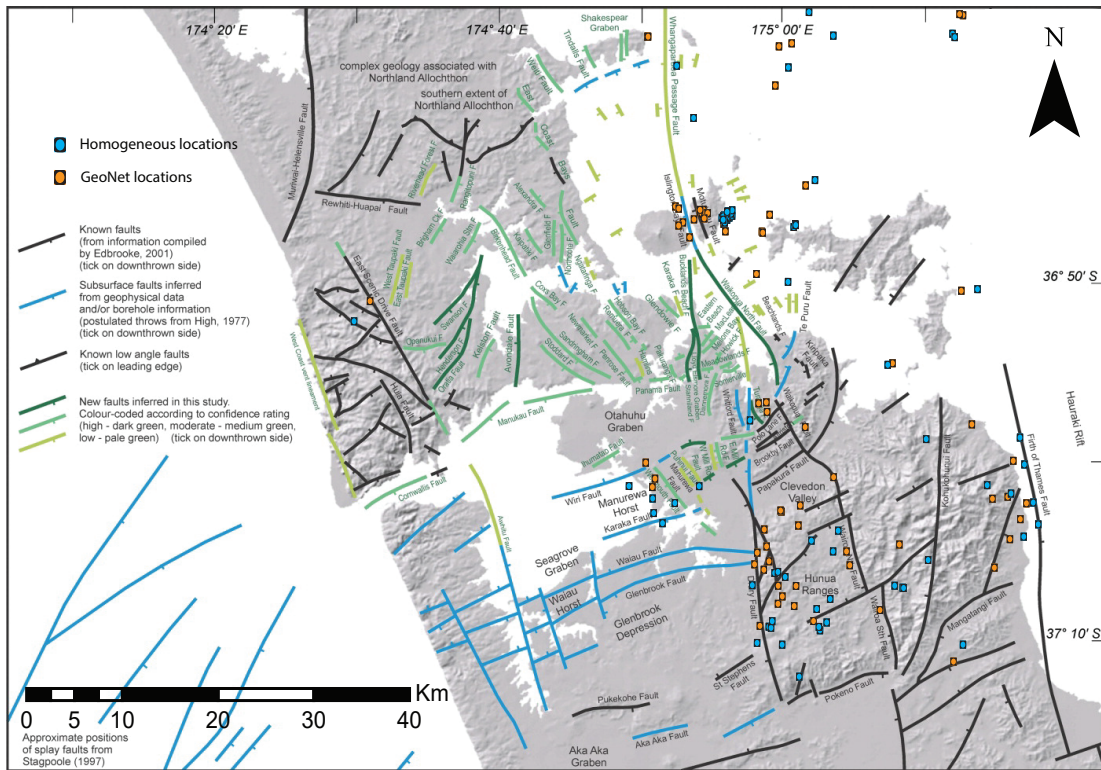
Figure 17: Post-Miocene fault map from Kenny et al. (2012), with GeoNet locations (orange) and those produced in this study using the homogeneous model (blue) superimposed. Only events reclassified as earthquakes are plotted.

Known faults within the Hauraki Gulf are not well constrained; however, Kenny et al. (2012) have interpreted the Whangaparoa Passage, Te Puru, and Islington Bay faults, for example, which have variable confidence ratings. No events relocated within the Hauraki Gulf reside on any mapped faults. However, it has produced two interesting results: the two events east of the Whangaparoa Passage fault, 2014p867461 and 2014p868169, and the five earthquakes proximal to Waiheke Island, 2012p001600, 2015p478371, 2015p478410, 2015p838179, and 2019p325466, which potentially manifest the offshore extension of the Te Puru fault (Figure 18). Interestingly, M1.8 earthquakes 2014p867461 and 2014p868169, previously labelled by GeoNet as quarry blasts, occurred in the days following event 2014p853608, an isolated M2.7 earthquake in the Rangitoto cluster. This seismicity follows a NW trend with time, approximating the orientation of the Whangaparoa Passage Fault, with events 2014p853608, 2014p867461 and 2014p868169 respect-

fully nucleating on the 12th, 17th, and 18th of November, 2014. Similarly, clustered earthquakes 2015p478371 (M2.5) and 2015p478410 (M2.2) occurred on the 26th and 27th of June 2015, while 2015p838179 (M1.5), annotated initially as a quarry blast, nucleated later that year on the 5th of November (Figures 16, 18).
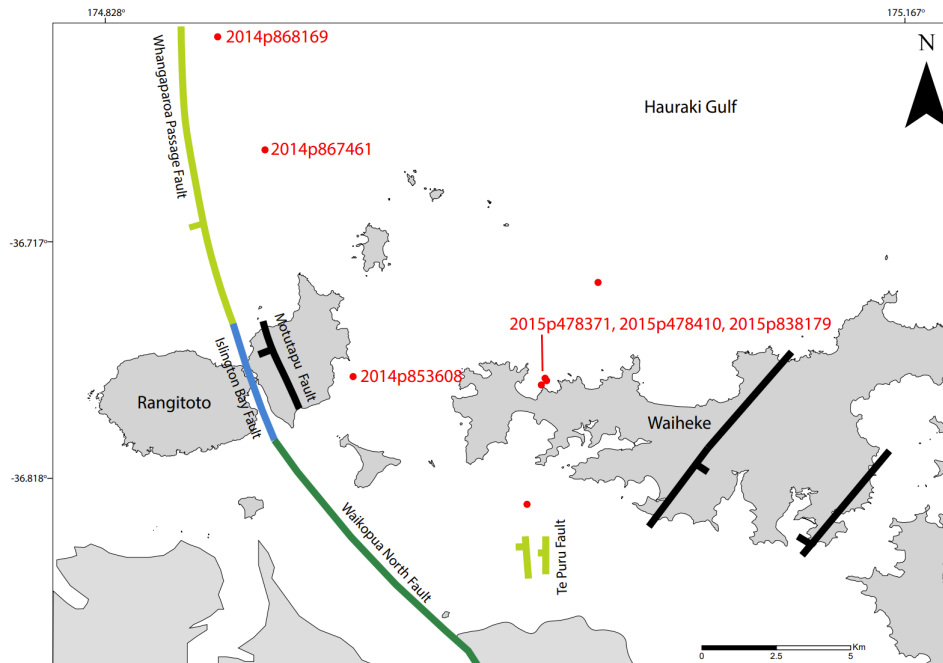
Figure 18: Map of earthquakes that could be associated with the Whangaparoa Passage, and Te Puru faults from Kenny et al. (2012). Earthquakes 2014p853608, 2014p867461 and 2014p868169 nucleated within a six day period, propagating SE-NW. Earthquakes 2015p478371 and 2015p478410 occurred within half an hour of each other, while 2015p838179 nucleated in the same cluster over four months later.

For eastern onshore Auckland, the GeoNet and homogeneous model locations have similar amounts of earthquakes proximal to faults; however events 2013p467376 (M1.4), 2016p104300 (M1.5), 2016p242523 (M1), and 2016p881685 (M1.3) are relocated to straddle the Firth of Thames Fault. Similarly, two earthquakes, 2016p560041 (M1.5) and 2016p560602 (M1.3), have migrated towards the northwards striking Kohukohunui Fault, both nucleating on the 26th of July, 2016, following a westward M1.1 earthquake earlier that day (2016p559812) (Figure 17).

5 Split Model

5.1 Homogeneous model station residuals

The homogeneous model produced in this study has reduced the RMS, constrained localities of clustered seismicity, and, through reclassification, seen temporally related seismic events, once assigned as quarry blasts, relocated to congregate parallel to interpreted faults. With several aims of this study achieved, one may stop their investigation. However, as announced, studies on the AVF have previously displayed a NNW-SSE trending split in crustal velocity, encouraging further interrogation of the dataset output by NonLinLoc (Ensing, 2020; Ensing et al., 2022; Ganefianto, 2018). With this, P-wave residuals at each station, for each event, have been plotted based on their size (Figure 19). Through misfit analysis, such data is theoretically sufficient to support or refute these previous observations.
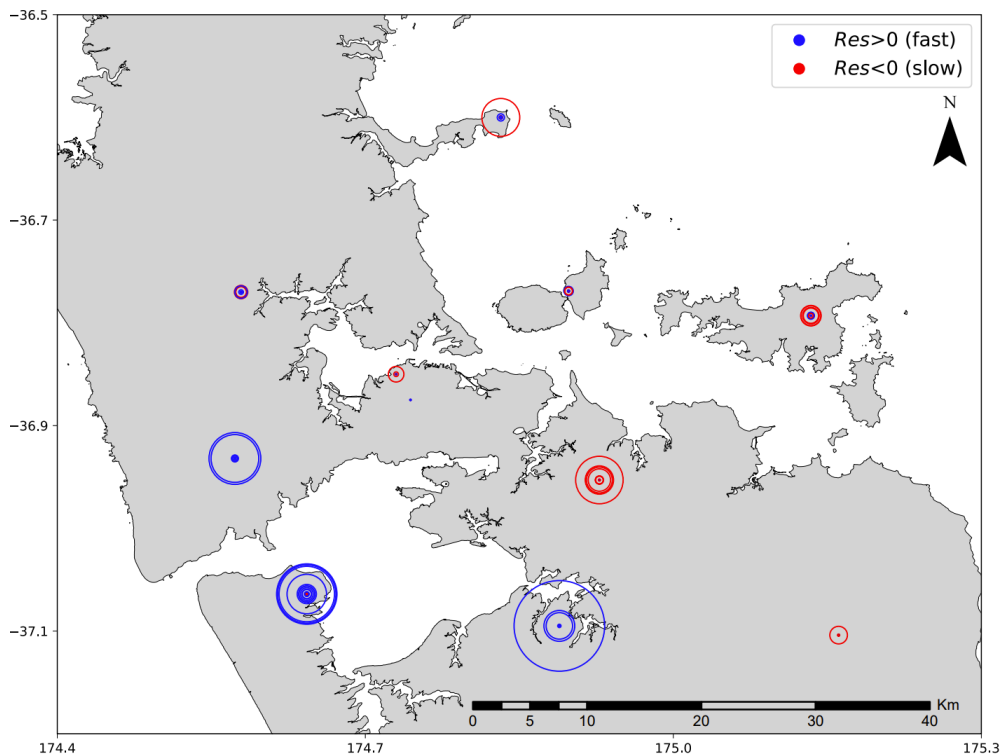
Figure 19: Plot of P-wave station residuals. Events contributing to this plot are selected as those with RMS < 0.1 s, showing that on average, P-waves arrive to the western stations later than the predicted rays (blue), but earlier than predicted to the eastern stations (red). The circle size represents the residual value, with the largest being 7.0 s (KBAZ), and the smallest 0 s (EPAZ, ETAZ, and MKAZ).

As expected, a story of two halves is presented, with the western stations characterised by predicted P-wave rays arriving sooner than the observed data: Res > 0 (Figure 19). While this insights that the western region requires a reduction in model velocity, the eastern stations indicate the converse, with predicted rays seeing too slow model velocities, arriving later than the observed data: Res < 0.

6 Discussion

6.1 Updated catalogue and event locations

Updating the catalogue of events within the defined criteria of this study, alongside their NonLin-Loc relocation using an optimised homogeneous model, has illuminated some significant findings regarding the AVF's seismicity.

The original GeoNet catalogue, consisting of 91 events, has been reduced to 86, with 14 unknown events and 10 quarry blasts reclassified as earthquakes based on their waveform morphologies. Furthermore, all P- and S-wave picks for the stations listed in Table 1 have been reviewed and expanded on. Despite GeoNet's manual review, many events, including those associated with the most significant release of seismic energy, such as M3.2 event 2013p203042, lacked distinctive S-wave picks, in addition to their P-wave arrival choices requiring refinement (Figure 3). Assuming that seismic arrivals have been chosen correctly, the advantage of using multiple phases rather than just P-waves for hypocentre locating has been well documented (e.g., Schöffel and Das, 1999). As such, this foreshadows that for GeoNet locations, even the largest magnitude events may have substantial location ambiguity – a crucial finding considering the microseismic nature of the AVF's catalogue, which is further evidenced by their average RMS of 0.403 ± 0.3 s (Figure 11; Table 4).

In conjunction with updating GeoNet's picks, this study has adapted several additional variables necessary for event location, which are likely to have shifted the spatial distribution of events in the iasp91 and homogeneous model relocations. For instance, the origin latitude and longitude used in the Transverse Mercator projection have been defined to neighbour the AVF. Similarly, unlike GeoNet, who use a minimum of 10 stations throughout their network when inverting for event location, this study has minimised the station data used to those exclusively within the AVSN

(Table 1) (GeoNet, n.d.). This was done regardless of the number of sensors with picks made, with the rationale being to have the best chance in identifying any local velocity heterogeneities truncating the AVF, such as the NW-SE trending split observed by Ensing (2020), Ensing et al. (2022) and Ganefianto (2018), which has been further supported in this study through station residuals (Figure 19).

Combined with technological advancements influencing GeoNet to have variable location methodologies through time, with both the iasp91 and nz3drx models respectively used in LOCSAT and NonLinLoc since 2012, these findings suggest that throughout New Zealand, once the relative event location has been found, perhaps more carefully reviewed picks could be run through specialised local velocity models (GeoNet, 2022). As displayed, this would provide more meaningful event locations, accentuating events clustered in space and time and improving qualitative interpretation of a given region's seismogenic zone structure. Such localised microseismic studies have been implemented along the Alpine Fault of New Zealand, for example, where probabilistic event location in NonLinLoc has aided the interpretation of the tectonic stress state and seismogenic crustal thickness (Boese et al., 2012).

For the AVF, such a model could start with the simplest possible 1D homogeneous model optimised in this study, or the iaps91 model given that seismicity appears to reside within its uppermost layer, extending to 20 km depth (Figures 8, 9; Table 2). However, more work is required to improve the depth estimates of these locations given that the average confidence ellipsoid semi-major axis is overwhelmingly orientated perpendicular to horizontal, at 091°- 271°(Figure 10). Although the average misfit produced by the homogeneous model has been significantly reduced relative to that of GeoNet, 0.118 ± 0.06 s is still larger than the estimated P- and S-wave uncertainties, respectively ± 0.02 s and ± 0.05 s (Table 4). Thus, as Figure 19, Ensing (2020) and Ensing et al. (2022) suggests, a more complex 3D split model will likely provide the required improvements. Such a model would be accepted if it reduced the average RMS, relocated earthquakes closer to known faults and quarry blasts to within quarries, and minimised the positive and negative residual bias between the western and eastern stations.

6.2 Spatiotemporal relationships: Homogeneous Model

A seismic tomography study proximal to the El Pilar Fault, the surface nucleating the Mw6.8 Cariaco earthquake in Venezuela, 1997 provides an analogy for this AVF investigation (Grosser et al., 2001). Originally, aftershocks associated with the rupture were located using a 1D average velocity model and, resultantly, found to reside 2-3 km north of where they would be expected. However, with velocities to the north of the lineament being 20% higher than those to the south, these events were relocated using a 3D model accounting for this lateral heterogeneity, with epicentres consequently shifted southwards to better coincide with known faults (Grosser et al., 2001). As emphasised here, and summarised by Havskov et al. (2011), when a sharp lateral discontinuity is present, such as that found by Ensing (2020) and Ensing et al. (2022) to truncate the AVF, epicentre locations are systematically displaced in the direction of higher velocity. Furthermore, with velocity generally increasing with depth, controlled by the increasing elastic parameters in Equations 5 and 6, this migration of event locations towards the higher velocity region becomes even more pronounced further within the lithosphere (Havskov et al., 2011).

Although this study has yet to tackle finding a more detailed model of the AVF, which will undeniably be the focus of succeeding investigations, such research provides meaning to discuss some of the spatiotemporal findings produced by the 1D homogeneous model. For instance, the eastern station residuals indicate that this region must be sped up relative to the west (Figure 19). For the Rangitoto earthquake cluster, it is, therefore, plausible that their relocation using a split model considering NW-SE lateral heterogeneity may bring these events closer to this volcanic island. Comparatively, the SE-NW, seemingly unilateral propagation of earthquakes 2014p853608, 2014p867461, and 2014p868169, could, once relocated using such a split model, migrate closer to the Waikopua North, Islington Bay and Whangaroa Passage fault system (Figure 18) (Kenny et al., 2012). For 2012p001600, 2015p478371, 2015p478410, 2015p838179, and 2019p325466, the same could be suggested, with these events likely to align better with the proposed offshore extension of the Te Puru fault, a fault recently confirmed by Gasston et al. (2021) to have accrued 60-100 m of vertical displacement.

6.2.1 Rangitoto clustered seismicity

With Rangitoto being the youngest edifice in the AVF, erupting ~ 500 cal. yrs. BP, the likelihood of the cluster of 19 events shifting closer to this volcano may seem alarming (Needham et al., 2011). However, given the limited spatial coverage of seismometers sampling the Hauraki Gulf, there are several possibilities for such seismicity, one of which has come to light in a soon-to-be-published self-potential (SP) study on this volcano (A. Luthfian, personal communication, November 24, 2023). These possibilities are:

1. Earthquake swarms associated with dike propagation events.

2. Fluids inducing repeating earthquakes to nucleate on the same fault patch.

3. Nonperiodic earthquakes attributed to intraplate fault stress release.

Suppose such shallow clustered seismicity, residing at 7.2 - 8.4 km depth, resulted from dike propagation. In that case, this finding may spark a further investigation by organisations like DEVORA, given the possibility of heightened volcanic hazard and risk to Auckland. México's Michoacán-Guanajuato monogenetic volcanic field provides an analogy for this scenario, where six distinct seismic swarms spanning 25 years are hypothesised to be precursors for a new eruption (Legrand et al., 2023). Like the 2013 events occurring within the Rangitoto cluster, which spanned 34 days and had the highest magnitude of 4, each of the six swarms in Michoacán-Guanajuato lasted for short periods of 1 - 2 months, with maximum magnitudes between 3.9 and 4.2 (Figure 14) (Legrand et al., 2023).

Despite the similarities with this case study in México, the waveforms of events within this cluster appear to have a tectonic signature (Figure 3). As such, A. Luthfian (personal communication, November 24, 2023) and L. Adam (personal communication, November 28, 2023) point out the recently found SP anomaly over the Rangitoto crater and the SP step-signal at the location of the Islington Bay fault, as mapped by Kenny et al. (2012). The narrow nature of the Rangitoto crater anomaly infers a shallow hydrothermal system, unlikely to be associated with the clustered seismicity at 7.2 - 8.4 km depth (L. Adam, personal communication, November 28, 2023). However, a CO_2 anomaly over the crater suggests degassing from a deep source, with the Islington Bay fault providing a possible fluid pathway. The finding of such fluid flow (H_2O and CO_2) insights

into the permeable and lubricated nature of this fault. As such, it is plausible for the cluster to be a location of repeating earthquakes affiliated with aseismic creep and slow slip (Uchida, 2019). For example, magnetotellurics have identified fluid migration from a low resistivity zone into the creeping portion of the San Andreas fault near Parkfield, a region also accustomed to repeated earthquakes (e.g., Becken et al., 2011; Chen et al., 2010).

Earthquake 2014p853608 resides within the Rangitoto agglomeration, manifesting the first event of three to propagate in a north-westerly azimuth parallel to the Islington Bay fault and extended Whangaparoa Passage fault (Figure 18)(Kenny et al., 2012). With this, the additional 18 events within the cluster could be associated with nonperiodic intraplate stress release without any specialised meaning. Support for this could be the homogeneous model revealing several other locations of multiple seismic events in the Hauraki Gulf, such as earthquakes 2015p478371, 2015p478410, and 2015p838179 near Waiheke (Figures 8, 18). As such, the identification of microseismicity within the Hauraki Gulf may be a function of the limited array of seismometers sampling this region. Nonetheless, geoscientists from New Zealand, China, and the USA have recently begun the installation of a temporary seismic array residing both onshore and offshore (K. van Wijk, personal communication, October, 2023). Such a network will inevitably increase the detection of microseismicity within the AVF, facilitating a 3D, high-resolution visualisation of the seismogenic zone and beyond.

6.3   Future work

As announced, concurrent with this study, groups of international geoscientists have been working to answer the million-dollar question of why monogenetic, intraplate volcanism exists in Auckland and what drives it. However, it has come to light in this study that a more detailed manual assessment may be required even for results already obtained, such as GeoNet's event locations and classifications.

Irrespective of the outcomes of this investigation, geophysicists at Te Herenga Waka – Victoria University of Wellington, have been actively utilising automatic picks made by EQTransformer, a machine learning algorithm (S. O'Hagan, personal communication, November 21, 2023) (Mousavi et al., 2020). They have been comparing these automated picks with their own manually selected

arrivals and those within GeoNet's catalogue. Using GaMMA, a phase association method using a Bayesian framework, they have already found orders of magnitude more events than available within GeoNet's catalogue, and will eventually run these through NonLinLoc (Zhu et al., 2022). Given that GeoNet currently requires automated picks on 10 stations for an event to be considered real, such research will help resolve the volume of microseismicity within the AVF (GeoNet, n.d.). With the homogeneous model reducing the average RMS, highlighting locations of clustered seismicity, and finding spatiotemporal patterns related to known faults, it could be used to locate such events while a 3D split velocity model is investigated. As outlined previously, such a complex model would only be accepted if it reduced the average RMS, minimised the positive and negative bias in the western and eastern station residuals, and located the epicentres of earthquakes and quarry blasts nearer to mapped faults and quarries, respectively.

Regarding event type, time- and frequency-domain analysis of the waveforms of events reclassified from quarry blasts to earthquakes could be implemented to examine whether this was justifiable. Horasan et al. (2009) successfully used this approach to decontaminate quarry blasts from a seismic catalogue in the Sea of Marmara, Turkey. In combination, moment tensor solutions could be obtained, from which focal mechanisms would be derived to isolate earthquakes from these explosions. The focal mechanism solutions for individual earthquakes would help constrain the faulting responsible for such seismicity and their possible strikes and dips. Furthermore, confirmed quarry blasts could be once again relocated with the z-coordinate held at 0 km during the inversion, as a more meaningful comparison of the homogeneous model and GeoNet blast locations could then be conducted (Figure 16).

In terms of the inversion itself, it would also be beneficial to compare the results obtained in this report with those produced if picks from stations TOZ, GRZ, and KUZ were utilised (Table 1). Incorporating these stations has the potential of reducing the model null space; however, on the contrary, it could complicate the interpretation of residuals, given the likelihood of introducing wider geological complexities outside of the AVF. Generating complete location *pdf* plots for both proposed homogeneous model runs would enhance our interpretation of the impacts of integrating the additional picks from these further afield stations. A relevant example is provided in Figure 20, courtesy of A. Lomax (personal communication, August 11, 2023) who confirmed the appropriate

input control file configuration of Appendix B to provide reasonable locations.
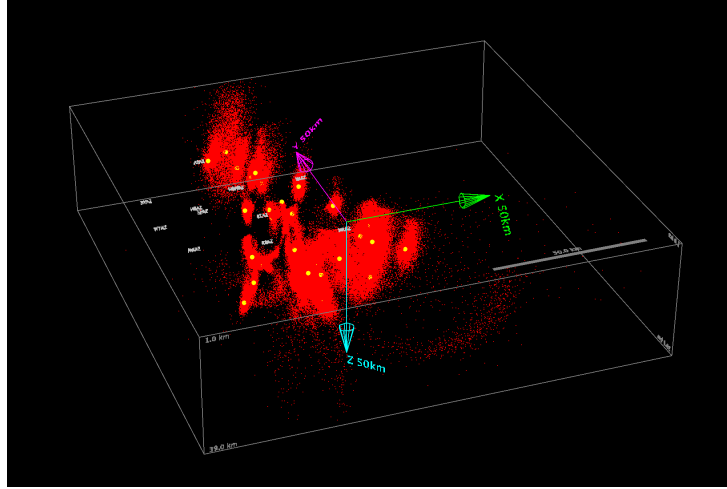
Figure 20: Compilation of the complete location *pdf*'s of events within the training dataset, using arbitrary model velocities, V_p and V_s. This plot is thanks to A. Lomax (personal communication, August 11, 2023) who assisted in setting up the input control file to ensure plausible locations. The red scatter clouds are the location *pdf*'s, while the yellow dots are the maximum likelihood hypocentres.

7   Conclusion

While this study of the AVF's seismicity has not tackled developing a high-resolution, 3D velocity model for the seismogenic crust, the revision of GeoNet's catalogue from 2012 to the present has unveiled some noteworthy findings that should be explored in subsequent research:

1. Despite GeoNet's manual review of most events within their catalogue, this study has rejected and reclassified several events. Additionally, even the largest magnitude earthquakes required refinements and additions to P- and S-wave picks. These findings indicate the necessity for a more thorough review of their automated STA/LTA events and picks by GeoNet.

2. Utilising NonLinLoc for the inversion of event locations and implementing the training, test, and validate split, this study indicates that the most representative, unbiased, homogeneous velocity model for the AVF is V_p = 5.94 km/s and V_s = 3.39 km/s. The average RMS of this model (0.118 ± 0.06 s) is significantly lower than the 0.403 ± 0.3 s from the original GeoNet catalogue, highlighting improved location accuracy.

3. Also produced in this study are locations of clustered seismicity and spatiotemporal patterns

related to known faults. The cluster of 19 events proximal to Rangitoto is perhaps the most significant finding. The development of a future split velocity model is likely to shift these earthquakes nearer to the Islington Bay Fault system. This is due to the same crustal dichotomy of previous tomography studies being found in the analysis of the eastern and western station residuals.

4. The study proposes several hypotheses for the causes of the Rangitoto earthquake cluster, influenced by a yet-to-be-published SP study. Given that Rangitoto is a consequence of the most recent eruptive activity in the AVF, dating to $\sim$500 cal. yrs. BP, further investigation of these events should be a primary focus of future studies.

Availability of data obtained

Within my GitHub linked below, I have attached all .obs files obtained in this investigation, as well as the .ipynb for the code given in Appendix A.

Click here to visit these resources.

References

Anaconda software distribution. (2022). https://docs.anaconda.com/

Ashenden, C., Lindsay, J., Steven, S., Smith, I., Craig, M., & Malin, P. (2011). Some challenges of monitoring a potentially active volcanic field in a large urban area: Auckland volcanic field, New Zealand. *Natural Hazards*, *59*(1), 507–528. https://www.proquest.com/docview/885907104#

Barter, S. (2021). *A study of lateral heterogeneity within the Auckland Volcanic Field during New Zealand's 2020 Covid-19 lockdown* (Honour's thesis). The University of Auckland.

Becken, M., Ritter, O., Bedrosian, P. A., & Weckmann, U. (2011). Correlation between deep fluids, tremor and creep along the central San Andreas fault. *Nature (London)*, *480*(7375), 87–90.

Beyreuther, M., Barsch, R., Krischer, L., Megies, T., Behr, Y., & Wassermann, J. (2010). ObsPy: A Python Toolbox for Seismology. *Seismological Research Letters*, *81*(3), 530–533. https://doi.org/10.1785/gssrl.81.3.530

Boese, C. M., Townend, J., Smith, E., & Stern, T. (2012). Microseismicity and stress in the vicinity of the Alpine Fault, central Southern Alps, New Zealand. *Journal of Geophysical Research: Solid Earth*, *117*(B2). https://doi.org/https://doi.org/10.1029/2011JB008460

Bradshaw, J. D. (1989). Cretaceous geotectonic patterns in the New Zealand Region. *Tectonics (Washington, D.C.)*, *8*(4), 803–820.

Chen, K. H., Bürgmann, R., Nadeau, R., Chen, T., & Lapusta, N. (2010). Postseismic variations in seismic moment and recurrence interval of repeating earthquakes. *Earth and Planetary Science Letters*, *299*(1), 118–125. https://doi.org/https://doi.org/10.1016/j.epsl.2010.08.027

Cole, J. W. (1990). Structural control and origin of volcanism in the Taupo volcanic zone, New Zealand. *Bulletin of Volcanology*, *52*(6), 445–459.

Deligne, N., Leonard, G., Jolly, A., Christenson, B., Hamling, I., Hreinsdottir, S., Mazcot, A., Miller, C., Roberts, R., & van Wijk, K. (2019). *DEVORA Novel Monitoring Techniques Workshop, 25 October 2018* (tech. rep.). GNS Science.

Eccles, J., Cassidy, J., Locke, C., & Spörli, K. (2005). Aeromagnetic imaging of the Dun Mountain Ophiolite Belt in northern New Zealand: insight into the fine structure of a major SW Pacific terrane suture. *Journal of the Geological Society*, *162*(4), 723–735. https://doi.org/10.1144/0016-764904-060

Edbrooke, S. (2001). Geology of the Auckland area. Institute of Geological Nuclear Sciences 1:250000 geological map 3. Lower Hutt, New Zealand. Institute of Geological Nuclear Sciences Limited. 1 sheet + 74 p.

Ensing, J. (2020). *Multi-Component Ambient Seismic Noise Tomography of the Auckland Volcanic Field* (PhD thesis). The University of Auckland.

Ensing, J., van Wijk, K., & Spörli, K. (2022). A 3D crustal shear speed model of the Auckland volcanic field, New Zealand, from multi-component ambient noise tomography. *Tectonophysics*, *845*, 229627. https://doi.org/https://doi.org/10.1016/j.tecto.2022.229627

Font, Y., Kao, H., Lallemand, S., Liu, C.-S., & Chiao, L.-Y. (2004). Hypocentre determination offshore Eastern Taiwan using the Maximum Intersection method [Geophysical Journal International, v. 158, n. 2, p. 655-675, 2004. http://dx.doi.org/10.1111/j.1365-246X.2004.02317.x]. *Geophysical Journal International*, *158*(2), 655–675. https://doi.org/10.1111/j.1365-246X.2004.02317.x

Ganefianto, G. (2018). *Seismic Travel Time Tomography of the Auckland Volcanic Field* (Master's thesis). The University of Auckland.

Gasston, C., Lindsay, J. M., Eccles, J. D., Brook, M., Hill, M., & Kenny, J. (2021). A geophysical and geomorphological investigation of large-offset normal faulting in Beachlands, Auckland. *New Zealand Journal of Geology and Geophysics*, *64*(1), 37–48.

GeoNet. (2022). The Aotearoa-New Zealand Earthquake Catalogue – A Potted History of Earthquake Location Meta-Data and Why It Matters. https://www.geonet.org.nz/news/5blJiT7KlLfwponxSFyWQD

GeoNet. (n.d.). Earthquake How. https://www.geonet.org.nz/earthquake/how

GNS Science. (2023). New Zealand Active Faults Database. https://data.gns.cri.nz/af/

Grosser, H., Rietbrock, A., Baumbach, M., Romero, G., & Rojas, J. (2001). Seismic Tomography in the Aftershock Region of the Cariaco Earthquake 1997. *AGU Fall Meeting Abstracts*, *-1*, 03.

Havskov, J., Bormann, P., & Schweitzer, J. (2011). Seismic source location. https://gfzpublic.gfz-potsdam.de/rest/items/item_43361/component/file_816919/content

Helmholtz-Centre Potsdam - GFZ German Research Centre for Geosciences and gempa GmbH. (2008). The SeisComP seismological software package. GFZ Data Services. https://doi.org/10.5880/GFZ.2.4.2020.003

Hopkins, J. L., Smid, E. R., Eccles, J. D., Hayes, J. L., Hayward, B. W., McGee, L. E., van Wijk, K., Wilson, T. M., Cronin, S. J., Leonard, G. S., Lindsay, J. M., Németh, K., & Smith, I. E. M. (2021). Auckland

Volcanic Field magmatism, volcanism, and hazard: a review. *New Zealand Journal of Geology and Geophysics*, *64*(2-3), 213–234.

Horasan, G., Boztepe Güney, A., Küsmezer, A., Bekler, F., Öğütçü, Z., & Musaoğlu, N. (2009). Contamination of seismicity catalogs by quarry blasts: An example from İstanbul and its vicinity, northwestern Turkey. *Journal of Asian earth sciences*, *34*(1), 90–99.

Horspool, N. A., Savage, M. K., & Bannister, S. (2006). Implications for intraplate volcanism and back-arc deformation in northwestern New Zealand, from joint inversion of receiver functions and surface waves. *Geophysical Journal International*, *166*(3), 1466–1483. https://doi.org/10.1111/j.1365-246X.2006.03016.x

Hunter, J. D. (2007). Matplotlib: A 2D Graphics Environment. *Computing in Science & Engineering*, *9*(3), 90–95. https://doi.org/10.1109/MCSE.2007.55

Huygens, C. (1690). *Traité de la Lumière*. Pieter van der Aa.

Kennett, B. L. N., & Engdahl, E. R. (1991). Traveltimes for global earthquake location and phase identification. *Geophysical Journal International*, *105*(2), 429–465.

Kenny, J. A., Lindsay, J. M., & Howe, T. M. (2012). Post-Miocene faults in Auckland: insights from borehole and topographic analysis. *New Zealand Journal of Geology and Geophysics*, *55*(4), 323–343. https://doi.org/10.1080/00288306.2012.706618

Legrand, D., Perton, M., Macías, J. L., Siebe, C., Pacheco, J., Chacón, F., Lermo, J., Quintanar, L., & Cisneros, G. (2023). Repeated seismic swarms near Paricutin volcano: precursors to the birth of a new monogenetic volcano in the Michoacán-Guanajuato volcanic field, México? *Bulletin of Volcanology*, *85*(5).

Leonard, G. S., Calvert, A. T., Hopkins, J. L., Wilson, C. J. N., Smid, E. R., Lindsay, J. M., & Champion, D. E. (2017). High-precision ^{40}Ar/^{39}Ar dating of Quaternary basalts from Auckland Volcanic Field, New Zealand, with implications for eruption rates and paleomagnetic correlations. *Journal of Volcanology and Geothermal Research*, *343*, 60–74. https://doi.org/10.1016/j.jvolgeores.2017.05.033

Lomax, A. (2005). A Reanalysis of the Hypocentral Location and Related Observations for the Great 1906 California Earthquake. *Bulletin of the Seismological Society of America*, *95*(3), 861–877. https://doi.org/10.1785/0120040141

Lomax, A., & Curtis, A. (2001). Fast probabilistic earthquake location in 3D models using Oct-Tree importance sampling. *Geophys. Res. Abstr.*, *3*.

Lomax, A., Michelini, A., & Curtis, A. (2009). Earthquake location, direct, global-search methods. https://api.semanticscholar.org/CorpusID:33693690

Lomax, A., Virieux, J., Volant, P., & Berge-Thierry, C. (2000). Probabilistic earthquake location in 3d and layered models. In C. H. Thurber & N. Rabinowitz (Eds.), *Advances in Seismic Event Location* (pp. 101–134). Springer Netherlands. https://doi.org/10.1007/978-94-015-9536-0_5

Luthfian, A., Eccles, J. D., & Miller, C. A. (2023). Gravity and magnetic models at Rangitoto Volcano, Auckland Volcanic Field, New Zealand: Implications for basement control on magma ascent. *Journal of Volcanology and Geothermal Research*, *439*, 107824. https://doi.org/https://doi.org/10.1016/j.jvolgeores.2023.107824

McGee, L., Smith, I., Millet, M.-A., Handley, H., & Lindsay, A. (2013). Asthenospheric control of melting processes in a monogenetic basaltic system: A case study of the auckland volcanic field, new zealand. *Journal of Petrology*, *54*(10), 2125–2153. https://doi.org/10.1093/petrology/egt043

Moser, T. J., van Eck, T., & Nolet, G. (1992). Hypocenter determination in strongly heterogeneous Earth models using the shortest path method. *Journal of Geophysical Research: Solid Earth*, *97*(B5), 6563–6572. https://doi.org/10.1029/91JB03176

Mousavi, S. M., Ellsworth, W. L., Zhu, W., Chuang, L. Y., & Beroza, G. C. (2020). Earthquake transformer—an attentive deep-learning model for simultaneous earthquake detection and phase picking. *Nature Communications*, *11*(1), 3952–3952.

Needham, A., Lindsay, J., Smith, I., Augustinus, P., & Shane, P. (2011). Sequential eruption of alkaline and sub-alkaline magmas from a small monogenetic volcano in the Auckland Volcanic Field, New Zealand. *Journal of Volcanology and Geothermal Research*, *201*(1), 126–142. https://doi.org/https://doi.org/10.1016/j.jvolgeores.2010.07.017

Podvin, P., & Lecomte, I. (1991). Finite difference computation of traveltimes in very contrasted velocity models: a massively parallel approach and its associated tools. *Geophysical Journal International*, *105*(1), 271–284. https://doi.org/10.1111/j.1365-246X.1991.tb03461.x

Schöffel, H.-J., & Das, S. (1999). Fine details of the Wadati-Benioff zone under Indonesia and its geodynamic implications. *Journal of Geophysical Research*, *104*(B6), 13, 101–13, 114. https://doi.org/10.1029/1999JB900091

Seebeck, H., Nicol, A., Giba, M., Pettinga, J., & Walsh, J. (2013). Geometry of the subducting Pacific plate since 20 Ma, Hikurangi margin, New Zealand. *Journal of the Geological Society*, *171*(1), 131–143. https://doi.org/10.1144/jgs2012-145

Snieder, R., & van Wijk, K. (2015). *A Guided Tour of Mathematical Methods for the Physical Sciences* (3rd ed.). Cambridge University Press.

Spörli, K., Black, P. M., & Lindsay, J. M. (2015). Excavation of buried Dun Mountain–Maitai terrane ophiolite by volcanoes of the Auckland Volcanic field, New Zealand. *New Zealand Journal of Geology and Geophysics*, *58*(3), 229–243. https://doi.org/10.1080/00288306.2015.1035285

Statistics New Zealand. (2018). Auckland Region. https://www.stats.govt.nz/tools/2018-census-place-summaries/auckland-region

Stein, S., & Wysession, M. (2013). *Introduction to Seismology*. Wiley-Blackwell.

Stern, R. J. (2002). Subduction zones. *Reviews of Geophysics*, *40*(4), 3-1-3–38.

Sutherland, R. (1999). Basement geology and tectonic development of the greater New Zealand region: an interpretation from regional magnetic data. *Tectonophysics*, *308*(3), 341–362.

Tarantola, A. (1987). *Inverse problem theory: Methods for data fitting and model parameter estimation*. Elsevier.

Tarantola, A., & Valette, B. (1982). Inverse problems = Quest for information. *Journal of Geophysics*, *50*, 159–170. https://api.semanticscholar.org/CorpusID:16323001

Toitū Te Whenua Land Information New Zealand. (n.d.). New Zealand Transverse Mercator 2000 (NZTM2000). https://www.linz.govt.nz/guidance/geodetic-system/coordinate-systems-used-new-zealand/projections/new-zealand-transverse-mercator-2000-nztm2000

Uchida, N. (2019). Detection of repeating earthquakes and their application in characterizing slow fault slip. *Progress in Earth and Planetary Science*, *6*(1), 1–21.

Wittlinger, G., Herquel, G., & Nakache, T. (1993). Earthquake location in strongly heterogeneous media. *Geophysical Journal International*, *115*(3), 759–777. https://doi.org/10.1111/j.1365-246X.1993.tb01491.x

Zeiler, C., & Velasco, A. A. (2009). Seismogram Picking Error from Analyst Review (SPEAR): Single-Analyst and Institution Analysis. *Bulletin of the Seismological Society of America*, *99*(5), 2759–2770. https://doi.org/10.1785/0120080131

Zhou, H.-w. (1994). Rapid 3-D hypocentral determination using a master station method. *Journal of Geophysical Research: Solid Earth*, *99*, 15439–15455. https://doi.org/10.1029/94JB00934

Zhu, W., McBrearty, I. W., Mousavi, S. M., Ellsworth, W. L., & Beroza, G. C. (2022). Earthquake Phase Association Using a Bayesian Gaussian Mixture Model. *Journal of Geophysical Research: Solid Earth*, *127*(5). https://doi.org/10.1029/2021jb023249

Appendices

A Code for P -and S-wave arrival picking

```
##The following code is developed to pick P- and S-wave arrivals on each station,
##for each event, placing these picks in an .obs file for use NonLinLoc.

##This is not a professional picker, but has rather been made by Kasper van Wijk and
#myself (Meegan Soulsby) as an educational piece to understand this process.

#Import packages required
import matplotlib
import matplotlib.pyplot as plt
from obspy.core import UTCDateTime
from obspy.clients.fdsn import Client
from matplotlib.dates import num2date
from obspy.core.event import Catalog, Event, Pick
from obspy.core.event.base import WaveformStreamID

#Setting up the backend that works for your device
matplotlib.use("TKAgg")

#Setting up the interactive selection of P- and S-wave arrival time picks

def onclick(event):
    ''' Record the times of the user's DOUBLE clicks on P- and S-wave arrivals in the
    global variable retval and close the figure '''
    if event.dblclick:
        global retval
        # save your picks to the retval list in UTCDateTime format. Note:
        # there must be a more elegant way than this:
        retval.append(UTCDateTime(num2date(event.xdata).isoformat()))
        # close the panel once  P- and an S-wave arrivals are picked:
        if len(retval) == 2:
            plt.close()


def makeapick(st_sttn,retval,phase):
    '''Make a pick for the event.
    INPUTS are the stream, the picks from clicks on the plot of the traces, and the phase of the wave (P or S).
    OUTPUT is the Pick() object pick.
    The following assumes that the first trace/pick is P and
    the second is S wave. '''
    pick = Pick()
    pick.phase_hint = phase
    if phase == 'P':
        seed_string = st_sttn[0].get_id()
        pick.waveform_id = WaveformStreamID(seed_string=seed_string)
        pick.time = retval[0]
    else:
        seed_string = st_sttn[1].get_id()
        pick.waveform_id = WaveformStreamID(seed_string=seed_string)
        pick.time = retval[1]
    return pick
```

50

```
##Defining parameters used for the Auckland Volcanic Field's (AVF) seismicity.


#The GeoNet database is used.
client= Client("GEONET")
net ='NZ'


#A string, converted to a list for the stations used to make hand-picked arrivals:
stn = 'ABAZ,AWAZ,EPAZ,ETAZ,GRZ,HBAZ,KBAZ,KUZ,MBAZ,MKAZ,MTAZ,RVAZ,TOZ,WIAZ,WTAZ'
stn_list = stn.split(',')


#Define the possible channels and loc of the stations of your catalogue:
chn ='HH*,EH*'
loc = '10,12'


#Define a start- and endtime to download within the Geonet catalogue
starttime=UTCDateTime("2012-01-01T00:00:01")
endtime = UTCDateTime.now()


#Define a box to look for events in the Geonet catalogue, and a minimum magnitude
[maxlat,minlat,minlon,maxlon,minmag] = [-36.5,-37.3,174.5,175.3,1.0]


#order your catalogue by descending orderby
orderby='magnitude'


##Generate a catalogue of events. Note, there were 91 events at the time of this study


events = client.get_events(starttime=starttime, endtime=endtime, minlatitude=minlat, maxlatitude=maxlat, minlongitude=minlon,
maxlongitude=maxlon, minmagnitude=minmag,orderby=orderby)
print(events)


#Define a new and empty catalog object:
cat = Catalog()
cat.description = "A catalogue with AVF events from Geonet but with only hand-picked arrivals"


##Picking on unfiltered waveform data


#Define the directory you wish to save your .obs files
writepath="/Users/meegansoulsby/documents/..."


#Loop through the events in the Geonet catalogue:
for event in events[0:2]: #Change this index in the square brackets. Can do all at once, or in stages.

    #Creating title for the output file as the GeoNet resource id
    title = str(event.resource_id).split('/')[1]

    #For every geonet event, create a new and empty event object to store the manual picks:
    e = Event()
    e.event_type = event.event_type

    #Download waveforms for the event in the Geonet catalogue:
    t0 = event.origins[0].time
    st = client.get_waveforms(network=net,station=stn,location=loc,channel=chn,starttime=t0,endtime=t0+40)

    #Plot the event on one station ( usually three channels) at a time:
    for sttn in stn_list:
```

```python
#Select the data stream per station:
st_sttn = st.select(station=sttn)

#Create an array for the new Pick objects:
retval = [] #these are mouse clicks

#Only continuing if there is a signal from this one station
if len(st_sttn)>0:

    #Plotting data for all channels available for this station
    fig,axs = plt.subplots(figsize=(15,15))
    st_sttn.plot(fig=fig)
    cid = fig.canvas.mpl_connect('button_press_event', onclick)
    plt.show()

    #If no picks are made, move into the next station. Do this by closing the window.
    if not retval:
        print('no picks, moving on to next station.')

    #If there is only one pick to make, this code assumes it is the P-wave arrival.
    #Make this pick and close the window.
    elif len(retval)==1:
        p = makeapick(st_sttn,retval,'P')

        #add the P wave pick to list of picks in the pick attribute of event e
        e.picks = e.picks+[p]

    #If there P and S picks made, retval is 2 and the next station will automatically pop up
    else:
        p = makeapick(st_sttn,retval,'P')
        s = makeapick(st_sttn,retval,'S')

        #Add the P and S wave picks to list of picks in the pick attribute of event e
        e.picks = e.picks+[p,s]

#Append the event to the new catalogue, IF it has picks:
if len(e.picks) > 0:
    cat.append(e)

    #Save .obs file for each event where you want them which was defined by writepath
    for event in cat:
        for pick in event.picks:
            event.write(writepath+title+"_handpicks"+".obs", format="NLLOC_OBS")
```

B NonLinLoc input control file

```
# Generic control file statements
# CONTROL - Control
CONTROL 1 54321


# TRANS - Geographic Transformation
TRANS TRANS_MERC GRS-80 -37.5 174.5 0.0


# Vel2Grid control file statements


# VGOUT - Output File Root Name
VGOUT  ./model_project/hom_model/hom_model


#  VGTYPE - Wave Type
VGTYPE P
VGTYPE S


# VGGRID - Grid Description
VGGRID  2 601 81  0.0 0.0 -1.0  0.5 0.5 0.5  SLOW_LEN


# velocity model description


#LAYER - Velocity Model - Layer
#Homogeneous Model AVF
#LAYER depth Vp_top Vp_grad Vs_top Vs_grad p_top p_grad
LAYER    -1.0    5.94   0    3.39      0


# Grid2Time control file statements


# GTFILES - Input and Output File Root Name
#GTFILES  ./model_project/hom_model/hom_model   ./time_project/hom_model/hom_model P   # uncomment to generate P travel times
GTFILES   ./model_project/hom_model/hom_model   ./time_project/hom_model/hom_model S  # uncomment to generate S travel times



# GTMODE - Program Modes
GTMODE GRID2D ANGLES_YES


# description of source (e.g. seismic station) for calculating travel-time field


# GTSRCE - Source Description
#Include your station text file with STSRCE statements, this line can be placed anywhere in control file
INCLUDE obs/AVF_station_coordinates.txt


# GT_PLFD - Podvin and Lecomte Finite Difference
GT_PLFD  1.0e-3  0


# NLLoc control file statements


# LOCSIG - Signature text
LOCSIG NonLinLoc - ALomax Scientific


# LOCCOM - Comment text
LOCCOM hom model


# LOCFILES - Input and Output File Root Name
```

```
LOCFILES ./run/merged_files_obs/*.obs  NLLOC_OBS  ./time_project/hom_model/hom_model  ./loc_project/hom_model/hom_model


# LOCHYPOUT - Output File Types
LOCHYPOUT SAVE_NLLOC_ALL NLL_FORMAT_VER_2 SAVE_HYPOINV_SUM


# LOCSEARCH - Search Type
LOCSEARCH  OCT 10 10 4 0.01 20000 5000 0 1


# LOCGRID - Search Grid Description
LOCGRID  151 151 41  0.0 0.0 -1.0  1.0 1.0 1.0  PROB_DENSITY SAVE


# LOCMETH - Location Method
LOCMETH EDT_OT_WT 9999.0 4 -1 -1 -9.99 6 -1.0 1


# LOCGAU - Gaussian Model Errors
LOCGAU 0.2 0.0


# LOCGAU2 - Travel-Time Dependent Model Errors
LOCGAU2 0.02 0.05 2.0


# LOCQUAL2ERR - Quality to Error Mapping
LOCQUAL2ERR 0.1 0.5 1.0 2.0 99999.9


# LOCANGLES - Take-off Angles parameters
LOCANGLES ANGLES_YES 5


# LOCPHSTAT - Phase Statistics parameters
LOCPHSTAT 9999.0 -1 9999.0 1.0 1.0 9999.9 -9999.9 9999.9
```